MASARYK UNIVERSITY

FACULTY OF SCIENCE

Hmotnostní distribuce v galaktických čočkách

Bachelor's Thesis

FILIP ZÁVADSKÝ

Brno, Spring 2026

MASARYK UNIVERSITY

FACULTY OF SCIENCE

Hmotnostní distribuce v galaktických čočkách

Bachelor's Thesis

FILIP ZÁVADSKÝ

Advisor: Henry James Best V, Ph.D.

Ústav teoretické fyziky a astrofyziky

Brno, Spring 2026

MUNI
SCI

Bibliografický záznam

Autor:	Filip Závadský Faculty of Science Masaryk University Ústav teoretické fyziky a astrofyziky
Název práce:	Hmotnostní distribuce v galaktických čočkách
Studijní program:	Fyzika
Studijní obor:	Astrofyzika
Vedoucí práce:	Henry James Best V, Ph.D.
Akademický rok:	2025/2026
Počet stran:	81
Klíčová slova:	gravitační čočky: silné, temná hmota, galaxie: jednotlivě: Cosmic Horseshoe (J1148+1930), galaxie: kinematika a dynamika

Bibliographic record

Author:	Filip Závadský Faculty of Science Masaryk University Department of Theoretical Physics and Astrophysics
Title of Thesis:	Mass distribution within galactic lenses
Degree Programme:	Physics
Field of Study:	Astrophysics
Supervisor:	Henry James Best V, Ph.D.
Academic Year:	2025/2026
Number of Pages:	81
Keywords:	gravitational lensing: strong, dark matter, galaxies: individual: Cosmic Horseshoe (J1148+1930), galaxies: kinematics and dynamics

Abstrakt

Vnitřní vlastnosti hal temné hmoty pravděpodobně ovlivňují vlastnosti galaxií, které se v nich nacházejí. Tato práce využívá přístup volného modelování ("free form moddeling") k modelování subhal temné hmoty v systému gravitační čočky J114833.1+193003.2, známém také jako Cosmic Horseshoe (Kosmická Podkova). Obrazová data byla získána z katalogu LaSTBeRu a jako modelovací software byla použita `Python` kniho vna `lenstromy`. Bylo testováno sedm různých kombinací tří běžných profilů čoček (SIS, SIE, EPL) s externím gravitačním smykovým napätím (external shear) a jedním světelným profilem (Sérsic elipse). Byly vzájemně porovnány na základě jejich redukovaného chí kvadrát χ^2_{red}. Jako nejlepší model se ukázala kombinace jednoho profilu EPL a pěti profilů SIS. Bylo vypočítáno prostorové rozložení hmoty i radiální rozložení hmoty pro modely s větším počtem čoček. Výsledky naznačují, že rozložení hmoty může být velmi asymetrické a že jsou potřebné další simulace s daty vyšší kvality. abstract

Abstract

Internal properties of dark matter halos are likely to impact the properties of galaxies located inside them. This work takes the free-form modeling approach to modeling dark matter subhalos in the galaxy-galaxy gravitational lens system J114833.1+193003.2, also know as the Cosmic Horseshoe. Image data were obtained from the LaSTBeRu catalagoue and the modeling software used is `lenstromy`. Seven different combinations of 3 common lens profiles (SIS, SIE, EPL), with external shear and one light profile (Sérsic Ellipse) were tested. They were compared against each other based on their χ^2_{red}. The best model was found to be a combination of 1 EPL and 5 SIS lens profiles. The spatial mass distribution as well as radial mass distribution for the models with more lens profiles were calculated. Results indicate that the mass distribution can be highly asymmetric and that further simulations with higher-quality data are desirable.

MUNI
SCI

MASARYKOVA UNIVERZITA
PŘÍRODOVĚDECKÁ FAKULTA
KOTLÁŘSKÁ 2, 611 37 BRNO
IČ: 00216224
DIČ: CZ00216224

ZADÁNÍ BAKALÁŘSKÉ PRÁCE

Akademický rok: 2025/2026

Ústav:	Ústav teoretické fyziky a astrofyziky
Student:	Filip Závadský
Program:	Fyzika
Specializace:	Astrofyzika

Ředitel *ústavu* PřF MU Vám ve smyslu Studijního a zkušebního řádu MU určuje bakalářskou práci s názvem:

Název práce:	Hmotnostní distribuce v galaktických čočkách
Název práce anglicky:	Mass distribution within galactic lenses
Jazyk práce:	angličtina

Oficiální zadání:
This topic will cover the basics of gravitational lensing to be used as a tool to study lensing galaxies with a focus on the Cosmic Horseshoe. The student will learn how matter impacts the propagation of light through the Universe, how these deflections can be used to probe the structure of galaxies using the Lenstronomy software, effective coding techniques, and Bayesian analysis using MCMC methods. The major outcome of this will be a Bachelor's thesis.

Vedoucí práce:	Henry James Best V, Ph.D.
Konzultant:	doc. RNDr. Michal Zajaček, Dr. rer. nat.
Datum zadání práce:	2. 10. 2025
V Brně dne:	1. 5. 2026

Zadání bylo schváleno prostřednictvím IS MU.

Filip Závadský, 30. 4. 2026
Henry James Best V, Ph.D., 30. 4. 2026
RNDr. Luboš Poláček, 30. 4. 2026

Acknowledgements

I sincerely thank my supervisor Henry James Best V, Ph.D. for the immense support during the entire thesis writing process. From the introduction to the beauty of lensing and lens modeling, to the checking of spelling mistakes and everything in between!! (such as kind comments, mental support, guidance and general introduction to academic workflow). I also thank my consultant doc. RNDr. Michal Zajaček, Dr. rer. nat. for that lucky beer at Astroparty which introduced me to my supervisor, as well as for the comments of the practical matters regarding this thesis. I would also like to thank my childhood astronomy club teacher Anna Veselovská for showing me the beauty of astronomy in general, along the sharing of the beautiful outlook on life. I also thank my parents for everything. Period. (and their continued support during my studies) I need to thank my friends and classmates, namely (in no particular order) JK, NK, NŽ, AZ, AT, JV, LB, JS, AP, LH, JP, KŠ, OK, SA, SH, TD, TD, PP, JD, MJ, MK, PŠ, JP, TČ for their mental and practical support during my studies and life. I am grateful to my good teachers, extended family, random people I met, and everyone who shaped me to be the person I am now! Last but not least, I also thank my girlfriend KK (for the patience and everything).

Declaration

Hereby I declare that this paper is my original authorial work, which I have worked out on my own. All sources, references, and literature used or excerpted during elaboration of this work are properly cited and listed in complete reference to the due source.

Filip Závadský

Contents

List of Tables

List of Figures

1 Introduction

Since the first theoretical derivations of dark matter, multitudes of papers and publications have been written on its nature and impact. Yet, such questions are far from successfully answered. This work tries to add its grain of sand to the mountains of already published works.

We will attempt to model the dark matter subhalos inside the galaxy-galaxy gravitational lens system J114833.1+193003.2 also known as the Cosmic Horseshoe. We will use image data from the LaSTBeRu and our modeling software of choice is the `Python` library `lenstronomy`. We will take the free-form modeling approach and allow our dark matter subhalos to freely move through the parameter space.

This work is structured as follows. Chapter 1 introduces the reader to the necessary theoretical concepts, most important of which is the existence of dark matter halos around galaxies (section 1.1) and the lensing theory needed for studying them (section 1.2). Chapter 2 describes our methodology: including the choice of our object, the lens modeling software, our modeling procedure and more. In chapter 3 we describe our results and try to draw conclusions from them in chapter 4. We would also like to direct the reader to the appendix A, where the resulting images of our fitting procedure are located.

1.1 Galaxies

Galaxies are known to be heterogeneous groups of objects. They vary significancy in terms of size, age, and morphology. However, all galaxies are believed to form inside of dark matter halos (Wechsler et al. 2018, Treu 2010). The growth, internal properties, and spatial distribution of galaxies are likely to be closely connected to the growth, internal properties, and spatial distribution of the dark matter halos they are a part of (Wechsler et al. 2018).

Dark matter makes up the largest fraction of mass of the galaxy (Aghanim et al. 2020). Within the radius of a dark matter halo, there may be multiple, distinct clumps of dark matter gravitationally bound to them. These are called subhalos as they are smaller than the host halo and they orbit within the gravitational potential of the host halo (Wechsler et al. 2018).

Figure 1.1: A lensing effect observed on the window of my dorm room

The distinguishing feature of dark matter is the fact that it interacts with the surrounding universe only via the gravitational force. It is therefore very difficult to observe dark matter directly. One of the tools which can be used to probe the dark matter (sub)structure is gravitational lensing.

1.2 Lensing

"A lens is anything that transmits light with some nontrivial optical path or light travel time, causing light deflection." (Saha et al. 2024) This is commonly observed in different artificial glass/plastic based lenses or drops of water. An example of such a lensing effect can be seen in figure 1.1. If, however, an interesting optical path is created by a gravitational field (more precisely due to the curvature of the spacetime metric), the resulting phenomenon is called gravitational lensing.

This work is concerned with "strong-lensing" (as opposed to "weak-lensing" and "microlensing"). Weak lensing is a phenomenon where light deflection and image distortions occur, but there are no additional images of the source (for a review of weak lensing see Schneider 2006), while microlensing is a temporary magnification of a source due to unresolvable strong lensing by very small objects (Vernardos et al. 2023) .

The following assumptions are usually made in strong lensing:

- geometrical optics are assumed for light sources and the gravitational lensing processes
- gravitational fields are assumed to be weak, such that light rays are deflected from straight lines only by very small angles. Contributions of many masses can be simply added (or integrated over) without the need to solve Einstein's field equations
- light deflection occurs over regions much smaller than the distances between light source, lensing mass, and observer (thin lens approximation)

1.2.1 The lens equation

At the heart of the lensing lies the so called "lens equation"

$$\vec{\beta} = \vec{\theta} - \vec{\alpha}(\vec{\theta}). \tag{1.1}$$

Lensing theory conventionality uses observer-centric coordinates. To an observer, a source appears to be located along a direction $\vec{\theta}$, whereas its true location is along some different direction $\vec{\beta}$. The directions $\vec{\theta}$ and $\vec{\beta}$ are two-dimensional angles on the sky (measured in radians or arc-seconds), while $\vec{\alpha}(\vec{\theta})$ is an apparent deflection angle (see, for example, Saha et al. 2024 or Wambsganss 1998)

1.2.2 Cosmological distances

Strong lensing is very difficult to observe nearby in the local Universe, but it is relatively common for galaxies at cosmological distances. For an in depth explanation of why this is the case, see the second chapter of Saha et al. 2024.

When working with lenses at cosmological distances, we need to account for the feature of our Universe called "expansion". It is desirable to refresh our memory of different ways for expressing distance.

The lookback time to some redshift z_{d} is given by

$$t_{\mathrm{d}} = \frac{1}{H_0} \int_{z_{\mathrm{d}}} \frac{\mathrm{d}z}{(1+z)E(z)}, \tag{1.2}$$

and ct_d is the distance traveled by light from the source to the observer (see Saha et al. 2024). The H_0 is the current expansion rate of the universe, the Hubble constant. The Hubble parameter $E(z)$ is given by

$$E(z) = \Omega_m(1+z^3) + \Omega_r(1+z^4) + \Omega_\Lambda, \tag{1.3}$$

where Ω_m is the current matter density fraction, Ω_r is the current relativistic energy-density fraction, and Ω_Λ is the "dark energy" density fraction. Through this work, we assume standard cosmological model (spatially flat), where $H_0 = 70$ km s^{-1} Mpc^{-1}, $\Omega_m = 0.3$ and $\Omega_\Lambda = 0.7$.

The comoving distance between two points along the line of sight at redshifts z_d and z_s is given by

$$\chi_\mathrm{ds} = \frac{c}{H_0}\int_{z_\mathrm{d}}^{z_\mathrm{s}} \frac{\mathrm{d}z}{E(z)}. \tag{1.4}$$

The angular diameter distance to the deflector (lens) and source is then

$$D_\mathrm{d} = \frac{\chi_\mathrm{d}}{1+z_\mathrm{d}}, \tag{1.5}$$

and

$$D_\mathrm{s} = \frac{\chi_\mathrm{s}}{1+z_\mathrm{s}}, \tag{1.6}$$

respectively. The angular diameter distance from the lens to source is

$$D_\mathrm{ds} = \frac{\chi_\mathrm{s} - \chi_\mathrm{d}}{1+z_\mathrm{s}}. \tag{1.7}$$

1.2.3 The source and lens plane

It is typical to approximate the regions where the lens and source are located as planes due to the cosmological distances separating them (see figure 1.2). The lens plane and source plane have redshifts z_d and z_s, respectively. The lens (deflector) is at angular diameter distance D_d from the observer so that an angle $\vec{\theta}$ on the observer's sky corresponds to a physical displacement $\vec{\xi}$ on the lens plane. Analogously, the source is at angular diameter distance D_s from the observer, and an angle $\vec{\beta}$ corresponds to a physical displacement $\vec{\eta}$ on the source plane. Projecting the distance to the source plane, we have the following

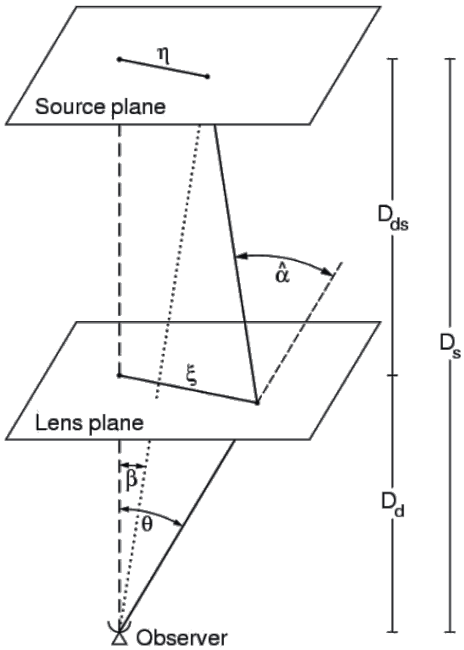

Figure 1.2: A diagram (reproduced from Saha et al. 2024) showing different lengths and angles used in the lensing formalism

relation:

$$D_s\vec{\beta} = D_s\vec{\theta} - D_{ds}\hat{\alpha}(\vec{\theta}), \tag{1.8}$$

and therefore

$$\vec{\beta} = \vec{\theta} - \frac{D_{ds}}{D_s}\hat{\alpha}(\vec{\theta}) \tag{1.9}$$

is our lens equation (1.1) generalized to the expanding universe. By introducing the apparent (scaled) deflection, we can make the lens equation into

$$\vec{\alpha} \equiv \frac{D_{ds}}{D_s}\hat{\alpha}(\vec{\theta}), \tag{1.10}$$

which makes equations (1.9) and (1.1) equivalent.

1.2.4 Einstein radius

In the circular-symmetric case, the deflection angle is given as

$$\hat{\alpha}(\vec{\xi}) = \frac{4GM(\xi)}{c^2}\frac{1}{\vec{\xi}}, \tag{1.11}$$

where $M(\xi)$ is the mass inside the radius ξ. For a point source lens of mass M, the deflection angle is therefore given by

$$\hat{\alpha}(\vec{\xi}) = \frac{4GM}{c^2}\frac{1}{\vec{\xi}}. \tag{1.12}$$

Plugging into equation 1.9 and using relation $\vec{\xi} = D_d\vec{\theta}$ (see figure 1.2), we obtain

$$\vec{\beta} = \vec{\theta} - \frac{D_{ds}}{D_s D_d}\frac{4GM}{c^2\vec{\theta}}. \tag{1.13}$$

For a case when the source lies exactly behind the lens ($\vec{\beta} = 0$), a ring-like image occurs whose angular radius is called the "Einstein radius" :

$$\theta_E = \sqrt{\frac{4GM}{c^2 D_d}\frac{D_{ds}}{D_s}}. \tag{1.14}$$

1.2.5 Convergence

Another way to write our lens equation 1.1 is by introducing the lens potential $\psi(\vec{\theta})$

$$\vec{\beta} = \vec{\theta} - \nabla\psi(\vec{\theta}). \tag{1.15}$$

The lens potential behaves as scaled version of a gravitational potential, and is the solution to the 2D Poisson equation

$$\nabla^2\psi(\vec{\theta}) = 2\kappa(\vec{\theta}), \tag{1.16}$$

where $\kappa(\vec{\theta})$ is the convergence, and is equivalent to the scaled mass density. The interested reader can find a more detailed explanation in Saha et al. 2024.

1.2.6 Shear

The cumulative deflection of light by all the other gravitational potentials along the line of sight are often represented by two additional free parameters, usually called "shear" or "external shear" (C. R. Keeton et al. 1997, Etherington et al. 2023).

2 Methodology

This chapter explains the source of our images (section 2.1), provides information about our particular object of interest (section 2.1.1), introduces our modeling software (section 2.2) along the optimization methods and their implementations (section 2.2.1 and 2.2.2), introduces the problem of multi-band fitting (section 2.3) and outlines the lens and light models used (section 2.4) along the particular combinations of them studied in later (section 2.5).

2.1 LaSTBeRu + particular surveys used

As a source of our image data, we used the "The Last Stand Before Rubin" (LaSTBeRu) (Alves de Oliveira et al. 2025). LaSTBeRu is a consolidated catalog of strong lensing systems, with a particular focus on galaxy-galaxy lensing. Not only does it provide results from the literature in one convenient place, but the image cutouts (20″ and 4′ in size) from various ground-based wide-field surveys (such as DESI Legacy (Dey et al. 2019), KiDS (KiDS and Astro-WISE Consortiums et al. 2013), DES (Collaboration 2005) and more) are available as well. It is currently the most extensive compilation of tabular data and ground-based imaging of known lenses.

2.1.1 J114833.1+193003.2 (Cosmic Horseshoe)

We chose a strong lensing system J114833.1+193003.2, colloquially known as the Cosmic Horseshoe, to perform our lens modeling as a proof of concept that subhalos may be detected. The Cosmic Horseshoe is located at $RA = 177.13808°$, $DEC = 19.50088°$. Another common designation for this object is SDSS J114833.14+193003.2. We chose the Cosmic Horseshoe because it is a lensing system with high degree of confidence, which forms an almost perfect Einstein ring. It is also well known in the field, which makes it easier to compare the results to the literature. A processed 20″ cutout of this system is shown in figure 2.1. Before the fitting procedure, we trimmed the edges (reduced the size of the image from 77 pixels to 49 pixels) to reduce background effects.

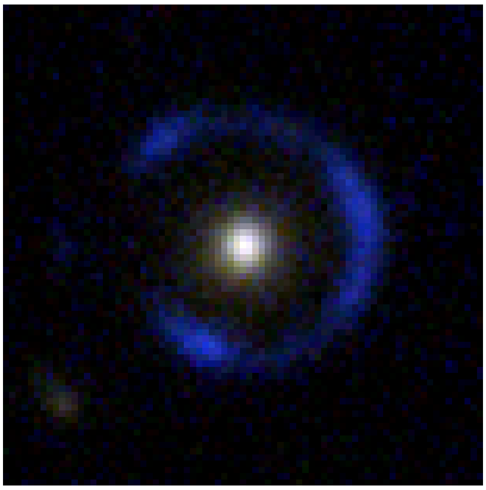

Figure 2.1: Processed cutout of the Cosmic Horseshoe from the DECam Legacy Survey (DECaLS) (Dey et al. 2019)

2.2 lenstronomy

We used `lenstronomy`[1], a multipurpose open-source `python`[2] (Rossum 1995) software package, designed to model strong gravitational lenses (Birrer and Amara 2018, Birrer, Shajib, et al. 2021). `Lenstronomy` supports a wide range of analytic lenses and light models in arbitrary combinations. `Lenstronomy` depends on packages included in `python` standard library, as well as proven open source libraries such as `numpy`[3], `scipy`[4], `astropy` (Astropy Collaboration et al. 2013), and `matplotlib` (Hunter 2007). For optimization and parameter inference routines, `CosmoHammer` (Akeret et al. 2013) is used, which supports Message Passing Interface (MPI) and allows for massive parallelization of `emcee` (Foreman-Mackey et al. 2013).

1. https://lenstronomy.readthedocs.io
2. https://www.python.org/
3. www.numpy.org
4. www.scipy.org

2.2.1 Particle Swarm Optimization (PSO)

According to Bonyadi et al. 2017, Particle swarm optimization (PSO) is a "stochastic population-based optimization method proposed by Eberhart et al. 1995".

In this work, particle swarm optimization was used for the calculation of a proper alignment fitting and as a precursor for the `emcee` in the main fitting sequence.

2.2.2 Monte Carlo Markov Chains (MCMC)

`emcee` (Foreman-Mackey et al. 2013) is a `Python` implementation of the the affine invariant ensemble sampler for Markov chain Monte Carlo (MCMC) proposed by Goodman et al. 2010. *emcee* was the main fitting routine used in this work.

2.3 Multiband fitting

`lenstronomy` is designed to simultaneously model lenses in multiple bands. We took advantage of this and used the `FittingSequence` class to model g, r, and z bands of our image cutouts simultaneously. The non-linear parameters (e.g. lens model or light profile shapes) are shared among the different bands. The linear parameters are optimized for each band individually, allowing for greater constraining power than any individual band.

2.3.1 Alignment fitting

Despite the fact that the images in different photometric bands are generally aligned, the precision of this alignment is usually insufficient. We used the `alignment_matching` module included in `lenstronomy` to overcome this issue.

2.4 Particular lens and light models used

In order to probe the lens substructure, we used 3 different relatively simple lens models, alongside external shear and one commonly used light model in various configurations. For a general overview of different lens models including more complex that were not used in this work, see for example Charles R. Keeton 2002.

2.4.1 Singular Isothermal Sphere (SIS)

`lenstronomy` defines the convergence of Singular Isothermal Sphere (SIS) as

$$\kappa(x,y) = \frac{1}{2}\left(\frac{\theta_E}{\sqrt{x^2+y^2}}\right), \tag{2.1}$$

where the θ_E is the Einstein radius and x, y are the positions in the image plane.

2.4.2 Singular Isothermal Ellipsoid (SIE)

Similarly, according to `lenstronomy` documentation, the Singular Isothermal Ellipsoid (SIE) has a convergence defined as:

$$\kappa(x,y) = \frac{1}{2}\left(\frac{\theta_E}{\sqrt{qx^2+y^2/q}}\right), \tag{2.2}$$

where θ_E is again the Einstein radius, q is the minor/major axis ratio, and x and y are defined in a coordinate system aligned with the major and minor axis of the lens.

2.4.3 Elliptic power law (EPL)

In `lenstronomy`, the Elliptical Power Law (EPL) is a mass profile with convergence defined as:

$$\kappa(x,y) = \frac{3-\gamma}{2}\left(\frac{\theta_E}{\sqrt{qx^2+y^2/q}}\right)^{\gamma-1}, \tag{2.3}$$

where θ_E is the Einstein radius, γ is the power-law slope of the 3D mass distributions, and similarly to SIE profile, q is the minor/major axis ratio, and x and y are defined in a coordinate system aligned with the major and minor axis of the lens.

Table 2.1: Number of free parameters for each lens configuration

Name	n_p
SIE	19
EPL	20
2SIE	24
2EPL	26
SIE + 5SIS	34
EPL + 5SIS	35
EPL + 50SIS	170

2.4.4 Shear (SHEAR)

In `lenstronomy` there is also a dedicated "lens profile" for simple expression of the external shear. The γ_1 and γ_2 define the relative strength and direction of the shear with respect to the image axes.

2.4.5 Sérsic Ellipse

The light profile used to model the lens light was an elliptical Sérsic function:

$$I(R) = I_e \exp\left(-b_n\left[(R/R_{\mathrm{Sersic}})^{\frac{1}{n}} - 1\right]\right), \tag{2.4}$$

where I_e is the intensity at the half light radius R_{Sersic}, with $R = \sqrt{qx^2 + y^2/q}$ and $b_n \approx 1.999n - 0.327$ (Sérsic 1963, Ciotti et al. 1999).

2.5 Our setup

We considered 7 different combinations of lens models. All of them included main lens profile (either SIE or EPL), external shear, one source light and one lens light profile (both provided by Sérsic Ellipse). Differences in models lied in the inclusions of various minor deflectors (provided by either SIE, EPL or SIS). The list of used models, as well as number of free parameters n_p, is provided in table 2.1.

3 Results

Our main goal was to consider if there is a meaningful distinction between using more lens profiles in galaxy-galaxy lens system or if just one is enough. We asses this by measuring the "goodness" of a particular fit, in other words, their χ^2_{red} value. Additional goals include trying to measure distance of the dark matter subhalos from the center of lens and to asses the possibility of finding asymmetry within the lens system and associated distribution of the dark matter subhalos.

3.1 Goodness of fits

The goodness of a particular fit is evaluated by the reduced χ^2 (which is defined such $\chi^2_{\text{red}} = \frac{\chi^2}{n_{\text{p}}}$, where n_{p} is the number of free parameters) values of the combined data, as well as the χ^2_{red} values for the individual image bands. This, as well as the sum of χ^2_{red} for all the data, is shown in table 3.1 (sorted by the χ^2_{red} value).

Table 3.1: χ^2_{red} for all tested configurations lens model configurations

	χ^2_{red}				
Lens model	Combined	g-band	r-band	z-band	Sum
SIE	-0.39980	0.39600	0.37710	0.42631	1.19941
EPL + 50SIS	-0.39795	0.39578	0.37694	0.42112	1.19384
2EPL	-0.39793	0.39340	0.37270	0.42768	1.19378
EPL	-0.39731	0.39405	0.37149	0.42640	1.19194
SIE + 5SIS	-0.39192	0.38351	0.36471	0.42755	1.17577
2SIE	-0.39014	0.38089	0.36801	0.42152	1.17041
EPL+5SIS	-0.38093	0.37044	0.35022	0.42213	1.14279

3.2 Asymmetry

The spatial distribution of perturbing lenses for different relevant models (SIE+5SIS, EPL+5SIS, EPL+50SIS) is presented in figures 3.1, 3.2 and 3.3. To better visualize the asymmetry caused by the additional

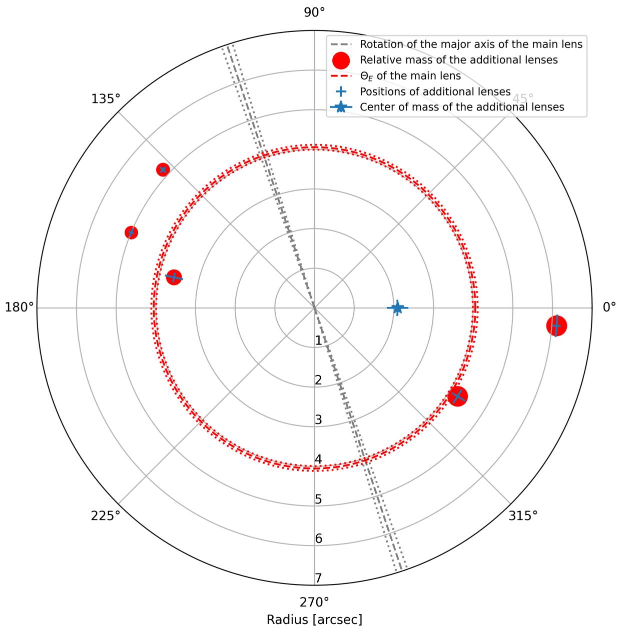

Figure 3.1: SIE + 5SIS model: Spatial distribution of perturbing lenses

lenses, we made these figures in polar coordinates. The origin coincides with the position of the center of the main lens. The Einstein radius θ_E of the main lens (either the SIE or EPL) is also included to help visualize the relative size of the main deflector.

3.3 Radial mass distribution

We resampled our results for the Einstein radius θ_E and distance r of our additional lenses using normal (Gaussian) distributions with standard deviation equal to our uncertainty. For each lens, we drew 5000 samples of θ_E and r pairs. This was done to better reflect the uncertainty of our fitting process and to have a more robust resulting mass distribution. The resulting relationship between mass of the additional lenses and radial distance from the center of the main lens, for the different relevant models (SIE+5SIS, EPL+5SIS, EPL+50SIS),

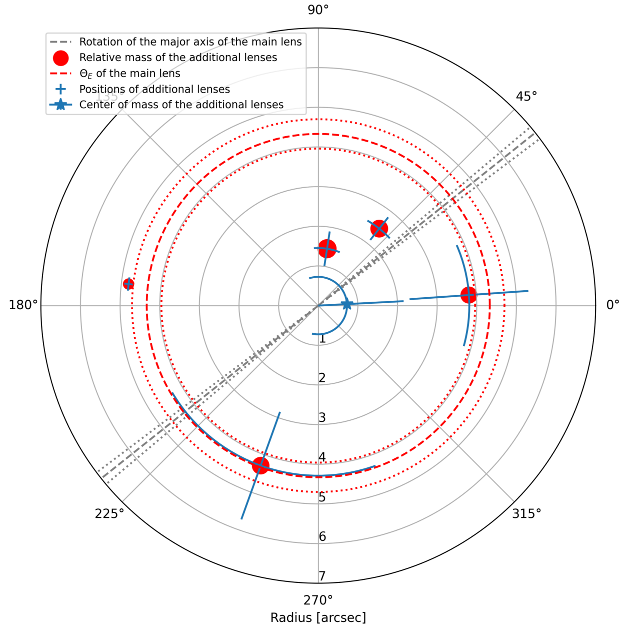

Figure 3.2: EPL + 5SIS model: Spatial distribution of perturbing lenses

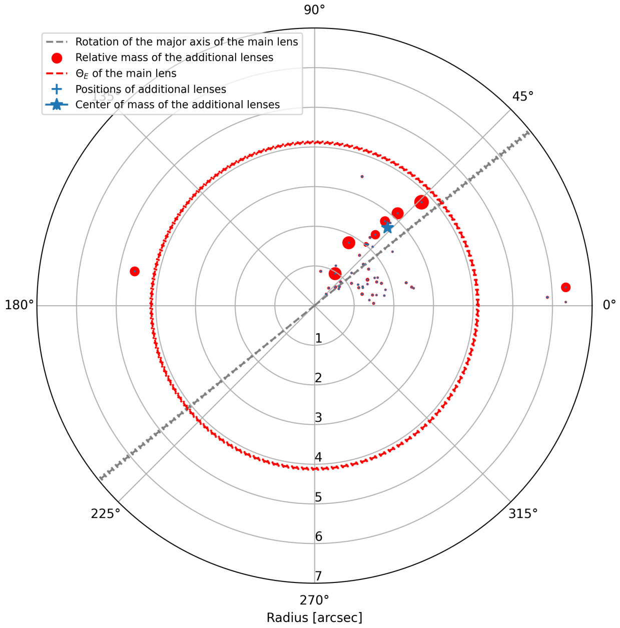

Figure 3.3: EPL + 50SIS model: Spatial distribution of perturbing lenses

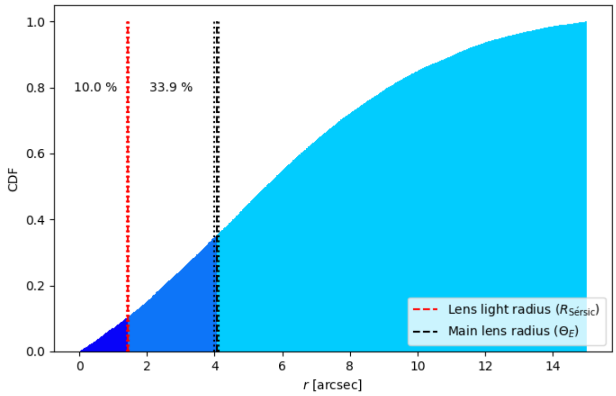

Figure 3.4: SIE + 5SIS model: Radial mass distribution of minor lenses.

given by the cumulative distribution function (CDF) of mass is illustrated in figures 3.4, 3.5 and 3.6. The lens light radius ($R_{\text{Sérsic}}$) and the main lens radius (θ_E) are marked with red and black vertical dashed lines, respectively. The relative mass percentage of the total subhalo mass within each radius are reported. This graph assumes that the position of center of the main lens radius and the position of the center of the lens light radius coincide.

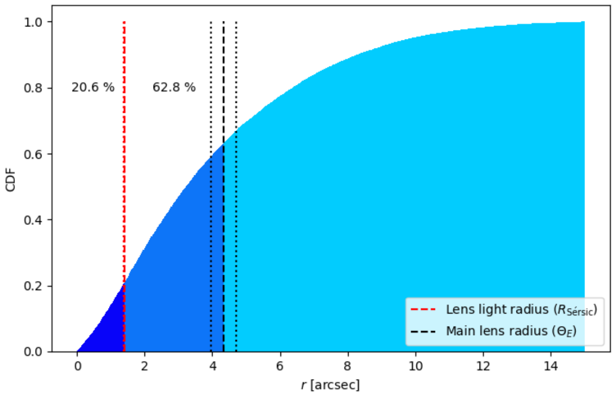

Figure 3.5: EPL + 5SIS model: Radial mass distribution of minor lenses

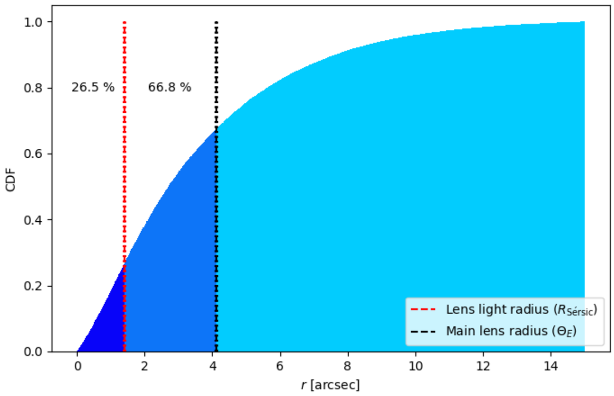

Figure 3.6: EPL + 50SIS model: Radial mass distribution of minor lenses

4 Conclusion

4.1 Determining the optimal model

We have fit our models to the Cosmic Horseshoe (J114833.1+193003.2) and compared them based on their χ^2_{red} (see table 3.1). The simple SIE model was found to have the highest χ^2_{red}, so we take that as a baseline (7th best). This is not surprising, since it is the model with the lowest number of free parameters ($n_{\text{P}} = 19$), and therefore has the least amount of freedom to probe the (asymmetric) mass distribution.

The 6th best is the EPL + 50SIS model. This model has theoretically the highest ability to model the asymmetric mass distribution, but the large amount of free parameters ($n_{\text{P}} = 170$) is penalized in the calculation of the χ^2_{red}.

The 2EPL (5th best) is a bit better, however, it is behind the simpler EPL (4th best). We think that this may be caused by the fact that the 2EPL model can probe a dipole mass distribution, but this is not enough to properly describe the lensing properties of our system. The added complexity of the 2EPL ($n_{\text{P}} = 26$) is penalized in the calculation of χ^2_{red}, while not providing enough benefit over the EPL ($n_{\text{P}} = 20$).

The top 1st, 2nd and 3rd results are provided by EPL+5SIS, 2SIE and SIE+5SIS models, respectively. Inclusion of the models with +5SIS in the best three, along with the fact that only in EPL+50SIS there are only few deflectors with a significant Einstein radii θ_E, suggests an existence of a few smaller dark matter subhalos alongside the main deflector. The fact that the EPL+5SIS model is best overall is likely caused by the better description of the mass distribution in the main lens due to the inclusion of the exponential γ parameter in EPL lens model (see equation 2.3), while still keeping a relatively small number of free parameters ($n_{\text{p}} = 35$).

4.2 Probing the asymmetry and radial mass distribution

For the models with additional smaller deflectors, we tried to quantify their position and asymmetry in the whole lens system caused by the additional mass (see section 3.2). In two of our models (EPL+50SIS and SIE+5SIS), the center of mass of the additional lenses does not coincide with the center of the main lens. In the third model with additional subhalos (EPL+5SIS), the center of the main lens lies within the uncertainty of the center of mass. This suggests that the spatial distribution of the additional mass subhalos can be highly asymmetric. However, higher quality imaging data and further simulations are need to lower the uncertainties on the position of the center of mass.

The radial mass distributions (see sections 3.3) for the EPL+5SIS and EPL+50SIS models show significantly higher mass percentage inside of the Einstein radius θ_E (62.8% and 66.8% respectively) compared to the SIE+5SIS model (33.9%). This is also true for the mass inside the lens light radius $R_{\text{Sérsic}}$ (20.6% and 26.5% respectively) compared to the SIE+5SIS model (10.0%). However, despite the difference in the mass within specific radii between models, it is also clear that the majority of the mass is outside of the lens light radius $R_{\text{Sérsic}}$. This suggests that the mass of the additional perturbers does not have a luminous counterpart and can be rightfully considered to be made of dark matter.

Table 4.1 contains a comparison between the results of our lens modeling (more precisely, the Einstein radius θ_E and external shear parameters γ_1 and γ_2) with those found in literature. The Einstein radius of our model is calculated as the sum of the Einstein radii of all lenses in the model. The symbol γ in the name of the model column (in the table labeled as "lens") denotes the inclusion of external shear. The abbreviation INT denotes Isaac Newton Telescope and HST is short Hubble Space Telescope. It is clear that our Einstein radii are bigger (except for the 2EPL model) than the typical values found in the literature. This may be caused mainly by the difference in the data quality (space vs. ground based telescope). Another explanation for this discrepancy could be the one described in Etherington et al. 2023, which is that the "external shear" is in many cases just a way to compensate for the lack of model complexity, and that it biases the other physically meaningful parameters.

Table 4.1: Comparison of the Einstein radii θ_E and external shear parameters γ_1 and γ_2 between literature (table reproduced from Bellagamba et al. 2016) and our results

	lens	source	data	θ_E	γ_1	γ_2
Dye et al. 2008	SIE+γ	-	INT	4.98	0.016	0.004
Dye et al. 2008	EPL+γ	-	INT	5.08	0.019	0.005
Kostrzewa-Rutkowska et al. 2014	SIE+γ	1 Sérsic	HST	5.08	0.019	-0.010
Newman et al. 2015	SIE+γ	1 Sérsic	HST	5.08	0.004	-0.022
Bellagamba et al. 2016	SIE+γ	1 Sérsic	HST	5.13	0.020	-0.021
Bellagamba et al. 2016	SIE+γ	5 Sérsic	HST	5.13	0.054	-0.019
Bellagamba et al. 2016	EPL+γ	5 Sérsic	HST	5.16	0.038	-0.038
this work	SIE+γ	1 Sérsic	DECam	5.71 ± 0.03	0.054 ± 0.005	0.262 ± 0.006
this work	EPL+50SIS+γ	1 Sérsic	DECam	5.36 ± 0.03	0.049 ± 0.003	0.202 ± 0.003
this work	2EPL+γ	1 Sérsic	DECam	3.5 ± 0.2	0.01 ± 0.01	-0.13 ± 0.02
this work	EPL+γ	1 Sérsic	DECam	5.71 ± 0.03	0.061 ± 0.005	0.299 ± 0.008
this work	SIE+5SIS+γ	1 Sérsic	DECam	5.70 ± 0.08	-0.049 ± 0.005	-0.025 ± 0.005
this work	2SIE+γ	1 Sérsic	DECam	5.7 ± 0.3	0.129 ± 0.008	0.21 ± 0.07
this work	EPL+5SIS+γ	1 Sérsic	DECam	5.9 ± 0.5	0.055 ± 0.008	0.24 ± 0.03

Dark matter makes up a significant portion of the matter inside our Universe. Lens modeling is one of the few ways of probing the dark matter. Our models point toward a presence of dark matter subhalos in the Cosmic Horseshoe. A majority of their mass is distributed outside the lens light radius ($R_{\text{Sérsic}}$), and around 30% of mass is located outside of the Einstein radius (θ_{E}) of the main lens. The distribution of these subhalos can be highly asymmetric as well. Our results of θ_{E} generally align with the literature, despite using data of poorer quality. In conclusion, we find that our method is a viable approach that should be further explored, with higher quality of data.

Bibliography

Aghanim, N. and et al. (Sept. 2020). “<i>Planck</i> 2018 results: VI. Cosmological parameters”. In: *Astronomy & Astrophysics* 641, A6. ISSN: 1432-0746. DOI: 10.1051/0004-6361/201833910. URL: http://dx.doi.org/10.1051/0004-6361/201833910.

Akeret, Joël et al. (Aug. 2013). “CosmoHammer: Cosmological parameter estimation with the MCMC Hammer”. In: *Astronomy and Computing* 2, pp. 27–39. ISSN: 2213-1337. DOI: 10.1016/j.ascom.2013.06.003. URL: http://dx.doi.org/10.1016/j.ascom.2013.06.003.

Alves de Oliveira, Renan et al. (Sept. 2025). “The Last Stand Before Rubin: a consolidated sample of strong lensing systems in wide-field surveys”. In: *arXiv e-prints*, arXiv:2509.09798. DOI: 10.48550/arXiv.2509.09798. arXiv: 2509.09798 [astro-ph.GA]. URL: https://arxiv.org/abs/2509.09798.

Astropy Collaboration et al. (Oct. 2013). “Astropy: A community Python package for astronomy”. In: 558, A33, A33. DOI: 10.1051/0004-6361/201322068. arXiv: 1307.6212 [astro-ph.IM].

Bellagamba, Fabio et al. (Oct. 2016). “Zooming into the Cosmic Horseshoe: new insights on the lens profile and the source shape”. In: *Monthly Notices of the Royal Astronomical Society* 464.4, pp. 4823–4834. ISSN: 1365-2966. DOI: 10.1093/mnras/stw2726. URL: http://dx.doi.org/10.1093/mnras/stw2726.

Birrer, Simon and Adam Amara (Dec. 2018). “lenstronomy: Multi-purpose gravitational lens modelling software package”. In: *Physics of the Dark Universe* 22, pp. 189–201. DOI: 10.1016/j.dark.2018.11.002. arXiv: 1803.09746 [astro-ph.CO].

Birrer, Simon, Anowar J. Shajib, et al. (2021). “lenstronomy II: A gravitational lensing software ecosystem”. In: *Journal of Open Source Software* 6.62, p. 3283. DOI: 10.21105/joss.03283. URL: https://doi.org/10.21105/joss.03283.

Bonyadi, Mohammad Reza et al. (Mar. 2017). “Particle Swarm Optimization for Single Objective Continuous Space Problems: A Review”. In: *Evolutionary Computation* 25.1, pp. 1–54. ISSN: 1063-6560. DOI: 10.1162/EVCO_r_00180. eprint: https://direct.mit.edu/evco/article-pdf/25/1/1/1535702/evco_r_00180.pdf. URL: https://doi.org/10.1162/EVCO_r_00180.

Ciotti, L. et al. (1999). *Analytical properties of the $R(1/m)luminositylaw$*. arXiv: astro-ph/9911078 [astro-ph]. URL: https://arxiv.org/abs/astro-ph/9911078.

Collaboration, The Dark Energy Survey (2005). *The Dark Energy Survey*. arXiv: astro-ph/0510346 [astro-ph]. URL: https://arxiv.org/abs/astro-ph/0510346.

Dey, Arjun et al. (Apr. 2019). "Overview of the DESI Legacy Imaging Surveys". In: *The Astronomical Journal* 157.5, p. 168. DOI: 10.3847/1538-3881/ab089d. URL: https://doi.org/10.3847/1538-3881/ab089d.

Dye, S. et al. (July 2008). "Models of the Cosmic Horseshoe gravitational lens J1004+4112". In: *Monthly Notices of the Royal Astronomical Society* 388.1, pp. 384–392. ISSN: 0035-8711. DOI: 10.1111/j.1365-2966.2008.13401.x. eprint: https://academic.oup.com/mnras/article-pdf/388/1/384/18722015/mnras0388-0384.pdf. URL: https://doi.org/10.1111/j.1365-2966.2008.13401.x.

Eberhart, R. et al. (1995). "A new optimizer using particle swarm theory". In: *MHS'95. Proceedings of the Sixth International Symposium on Micro Machine and Human Science*, pp. 39–43. DOI: 10.1109/MHS.1995.494215.

Etherington, Amy et al. (2023). *Strong gravitational lensing's 'external shear' is not shear*. arXiv: 2301.05244 [astro-ph.CO]. URL: https://arxiv.org/abs/2301.05244.

Foreman-Mackey, Daniel et al. (Mar. 2013). "emcee: The MCMC Hammer". In: 125.925, p. 306. DOI: 10.1086/670067. arXiv: 1202.3665 [astro-ph.IM].

Goodman, Jonathan R et al. (2010). "Ensemble samplers with affine invariance". In: URL: https://api.semanticscholar.org/CorpusID:54842399.

Hunter, J. D. (2007). "Matplotlib: A 2D graphics environment". In: *Computing in Science & Engineering* 9.3, pp. 90–95. DOI: 10.1109/MCSE.2007.55.

Keeton, C. R. et al. (June 1997). "Shear and Ellipticity in Gravitational Lenses". In: *The Astrophysical Journal* 482.2, pp. 604–620. ISSN: 1538-4357. DOI: 10.1086/304172. URL: http://dx.doi.org/10.1086/304172.

Keeton, Charles R. (2002). *A Catalog of Mass Models for Gravitational Lensing*. arXiv: astro-ph/0102341 [astro-ph]. URL: https://arxiv.org/abs/astro-ph/0102341.

KiDS and Astro-WISE Consortiums et al. (Jan. 2013). "The Kilo-Degree Survey". In: *Experimental Astronomy* 35.1, pp. 25–44. ISSN: 0922-6435, 1572-9508. DOI: 10.1007/s10686-012-9306-1. URL: http://link.springer.com/10.1007/s10686-012-9306-1 (visited on 04/20/2026).

Kostrzewa-Rutkowska, Zuzanna et al. (July 2014). "The evolution of late-type galaxies from CASSOWARY lensing systems". In: *Monthly Notices of the Royal Astronomical Society* 441.4, pp. 3238–3248. ISSN: 0035-8711. DOI: 10.1093/mnras/stu783. eprint: https://academic.oup.com/mnras/article-pdf/441/4/3238/4051632/stu783.pdf. URL: https://doi.org/10.1093/mnras/stu783.

Newman, Andrew B. et al. (Sept. 2015). "LUMINOUS AND DARK MATTER PROFILES FROM GALAXIES TO CLUSTERS: BRIDGING THE GAP WITH GROUP-SCALE LENSES". In: *The Astrophysical Journal* 814.1, p. 26. DOI: 10.1088/0004-637X/814/1/26. URL: https://doi.org/10.1088/0004-637X/814/1/26.

Rossum, Guido (1995). *Python reference manual*. Tech. rep. NLD.

Saha, Prasenjit et al. (2024). *Essentials of strong gravitational lensing*. arXiv: 2401.04165 [astro-ph.CO]. URL: https://arxiv.org/abs/2401.04165.

Schneider, P. (2006). "Weak Gravitational Lensing". In: *Gravitational Lensing: Strong, Weak and Micro*. Springer Berlin Heidelberg, pp. 269–451. ISBN: 9783540303107. DOI: 10.1007/978-3-540-30310-7_3. URL: http://dx.doi.org/10.1007/978-3-540-30310-7_3.

Sérsic, J. L. (Feb. 1963). "Influence of the atmospheric and instrumental dispersion on the brightness distribution in a galaxy". In: *Boletin de la Asociacion Argentina de Astronomia La Plata Argentina* 6, pp. 41–43.

Treu, Tommaso (Aug. 2010). "Strong Lensing by Galaxies". In: *Annual Review of Astronomy and Astrophysics* 48.1, pp. 87–125. ISSN: 1545-4282. DOI: 10.1146/annurev-astro-081309-130924. URL: http://dx.doi.org/10.1146/annurev-astro-081309-130924.

Vernardos, G. et al. (2023). *Microlensing of strongly lensed quasars*. arXiv: 2312.00931 [astro-ph.GA]. URL: https://arxiv.org/abs/2312.00931.

Wambsganss, Joachim (Dec. 1998). "Gravitational Lensing in Astronomy". In: *Living Reviews in Relativity* 1.1, p. 12. ISSN: 2367-3613, 1433-

8351. DOI: 10.12942/lrr-1998-12. URL: http://link.springer.com/10.12942/lrr-1998-12 (visited on 04/13/2026).

Wechsler, Risa H. et al. (Sept. 2018). "The Connection Between Galaxies and Their Dark Matter Halos". In: *Annual Review of Astronomy and Astrophysics* 56.1, pp. 435–487. ISSN: 1545-4282. DOI: 10.1146/annurev-astro-081817-051756. URL: http://dx.doi.org/10.1146/annurev-astro-081817-051756.

Index

A Pretty Images

This appendix shows the representation of each lens model during the reconstruction process. The "reconstructed source" do not appear to be not well captured, but note the very small length scale (0.1" instead of the 1" typical for other images). This may be caused either by the source galaxy's morphology not being properly modeled by the Sérsic profile, or by the small scale not providing enough detail. This is not of concern for our needs, because the reconstruction seems to consistent across models.

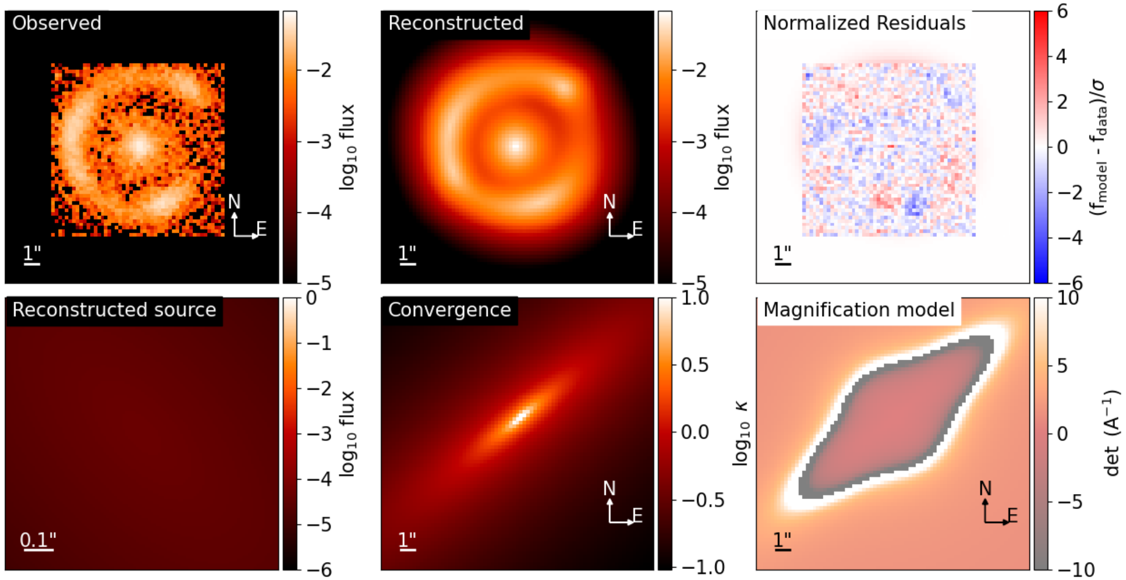

Figure A.1: SIE model, g-band: Comparison of observed and reconstructed images, as well as the residuals, reconstructed source, convergence and the magnification model for different image bands

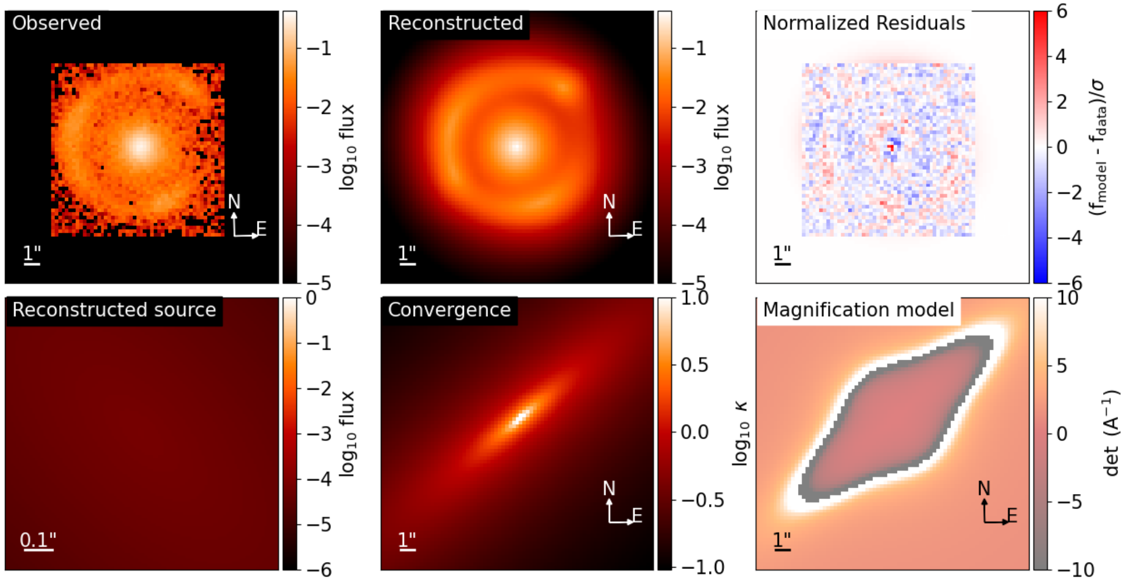

Figure A.2: SIE model, r-band: Comparison of observed and reconstructed images, as well as the residuals, reconstructed source, convergence and the magnification model for different image bands

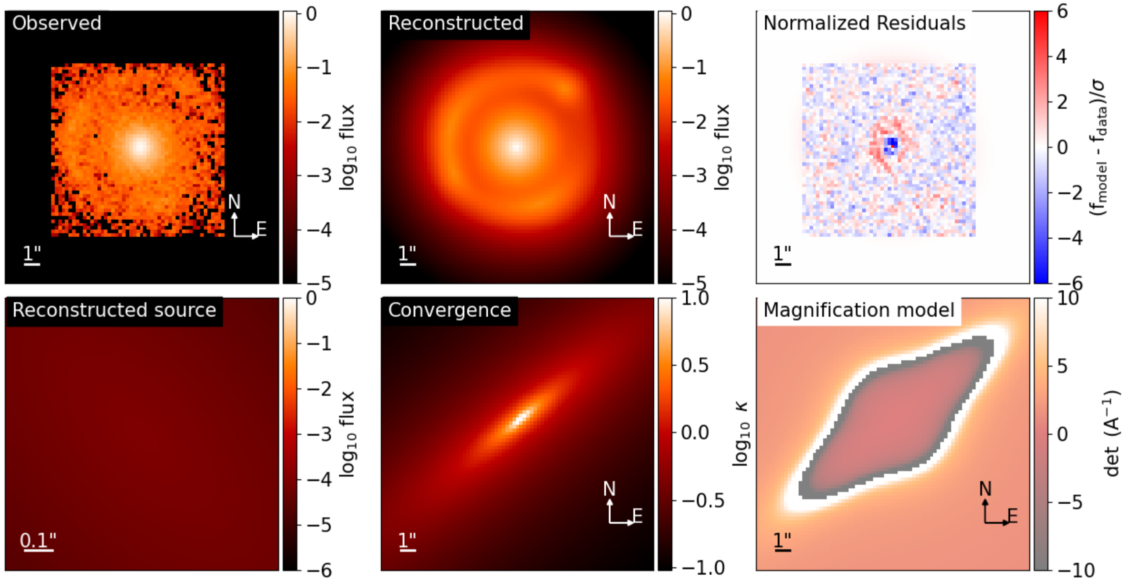

Figure A.3: SIE model, z-band: Comparison of observed and reconstructed images, as well as the residuals, reconstructed source, convergence and the magnification model for different image bands

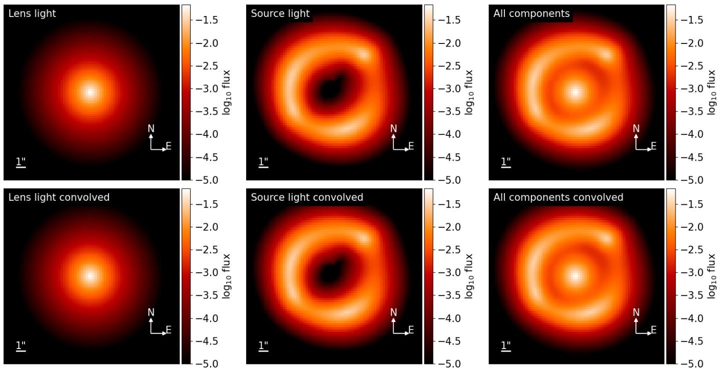

(a) *g*-band

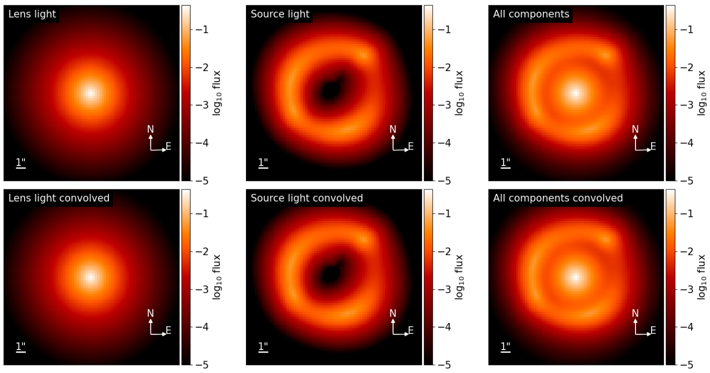

(b) *r*-band

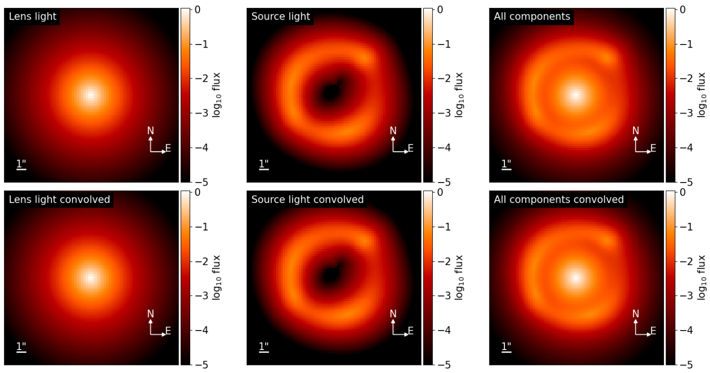

(c) *z*-band

Figure A.4: SIE model: Lens light, source lights and their convolutions for different image bands

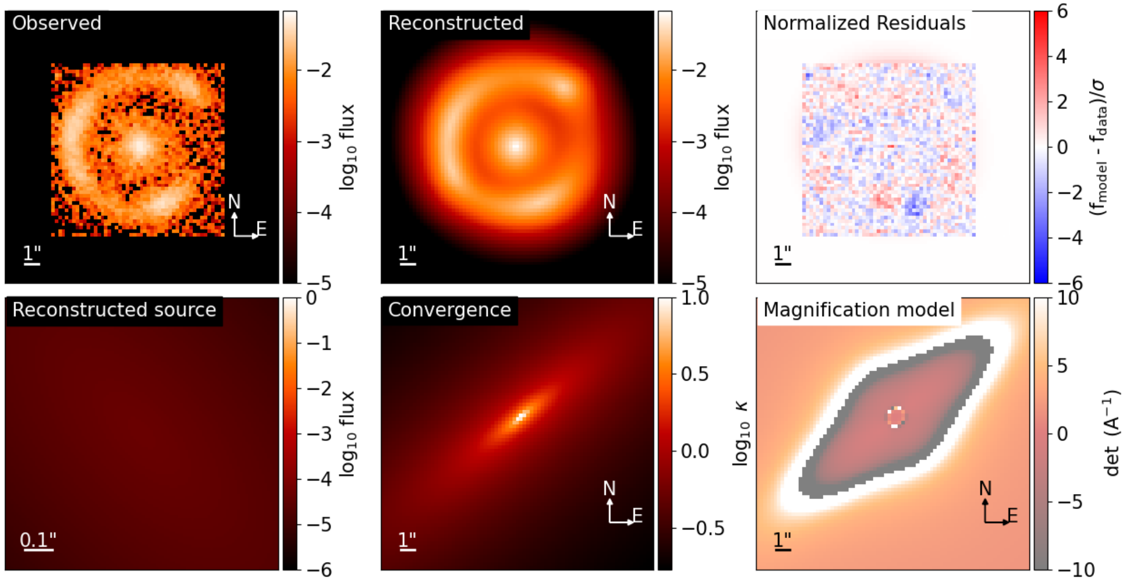

Figure A.5: EPL model, *g*-band: Comparison of observed and reconstructed images, as well as the residuals, reconstructed source, convergence and the magnification model for different image bands

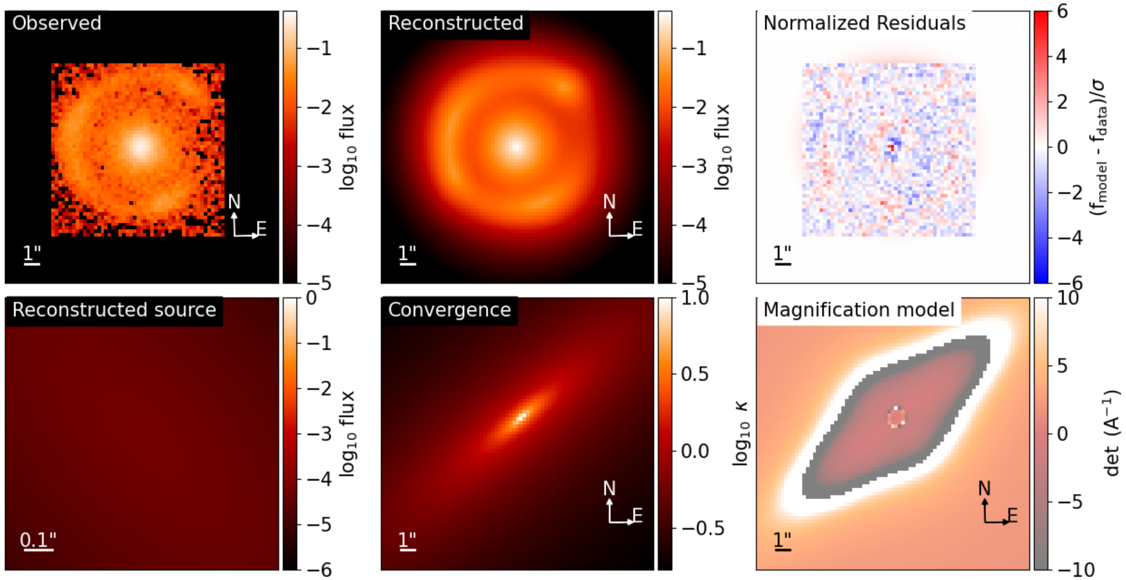

Figure A.6: EPL model, *r*-band: Comparison of observed and reconstructed images, as well as the residuals, reconstructed source, convergence and the magnification model for different image bands

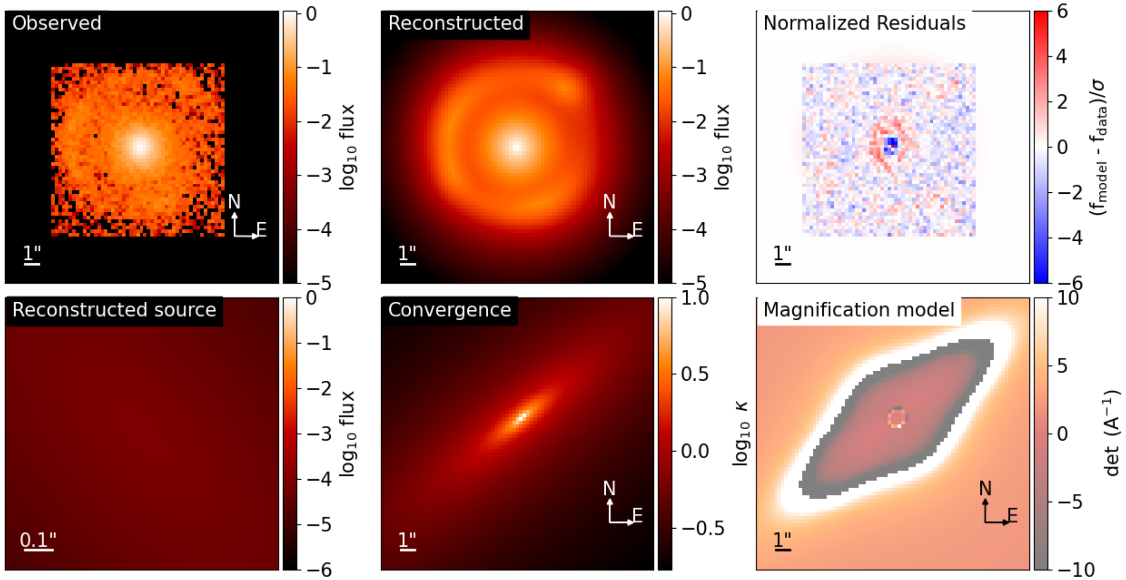

Figure A.7: EPL model, z-band: Comparison of observed and reconstructed images, as well as the residuals, reconstructed source, convergence and the magnification model for different image bands

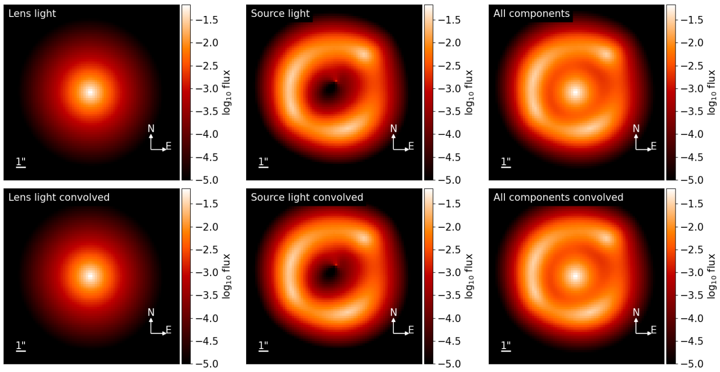

(a) g-band

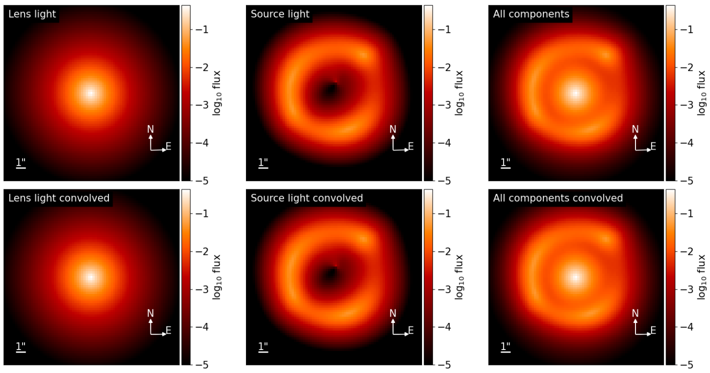

(b) r-band

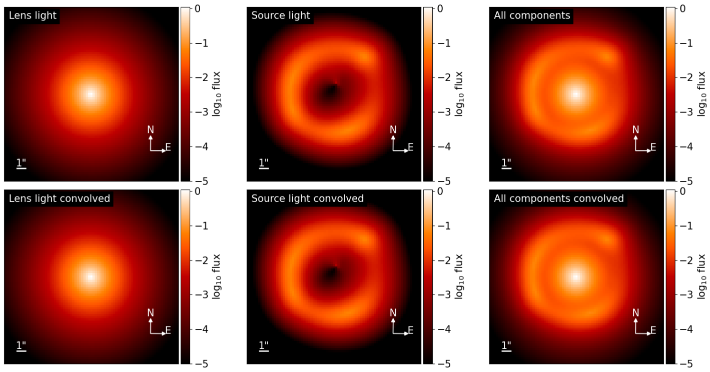

(c) z-band

Figure A.8: EPL model: Lens light, source lights and their convolutions for different image bands

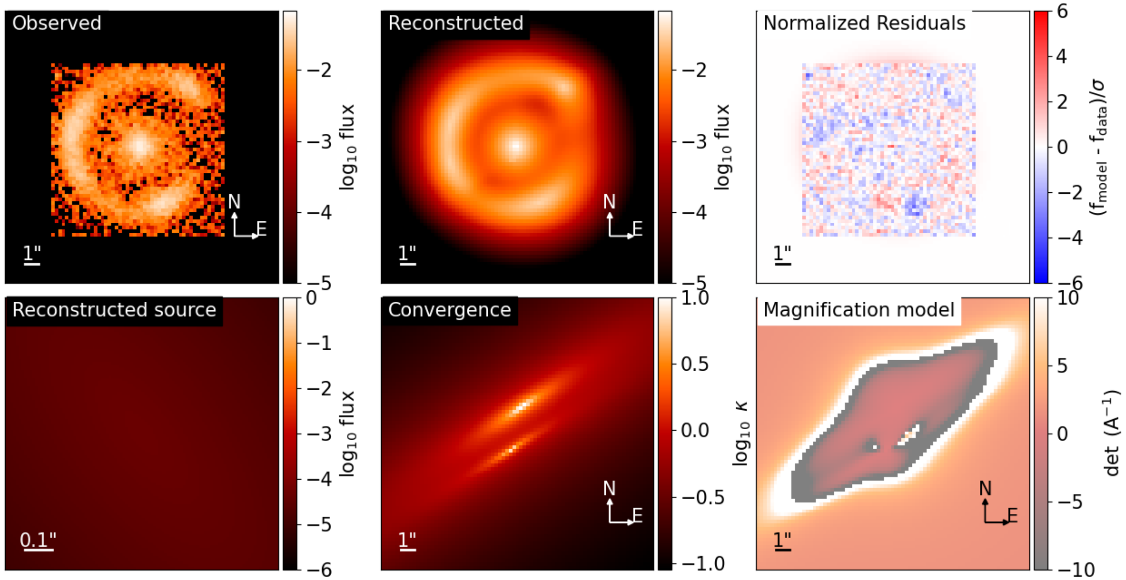

Figure A.9: 2SIE model, *g*-band: Comparison of observed and reconstructed images, as well as the residuals, reconstructed source, convergence and the magnification model for different image bands

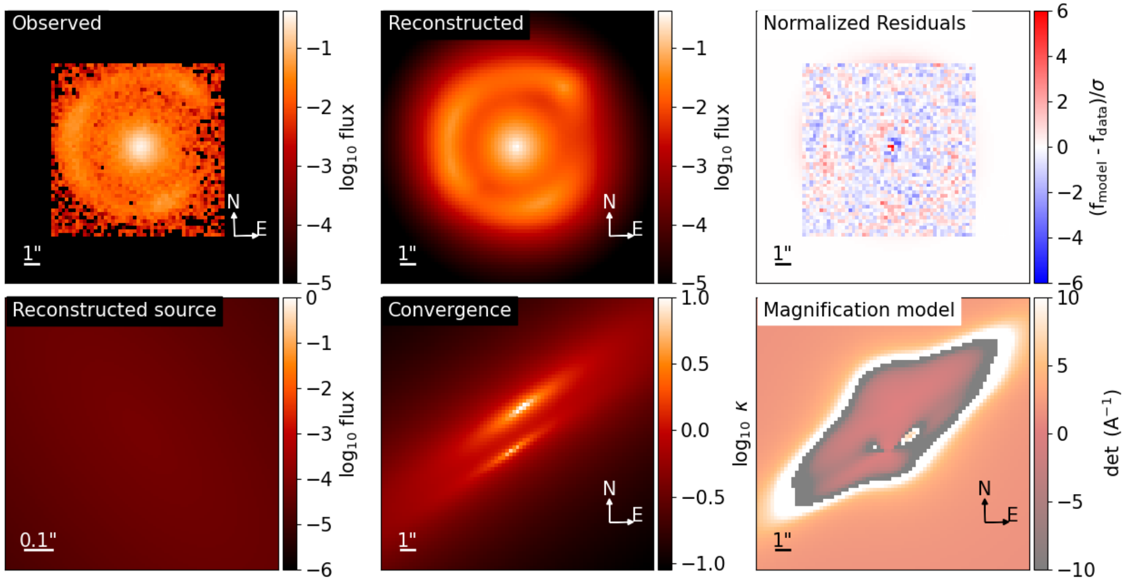

Figure A.10: 2SIE model, *r*-band: Comparison of observed and reconstructed images, as well as the residuals, reconstructed source, convergence and the magnification model for different image bands

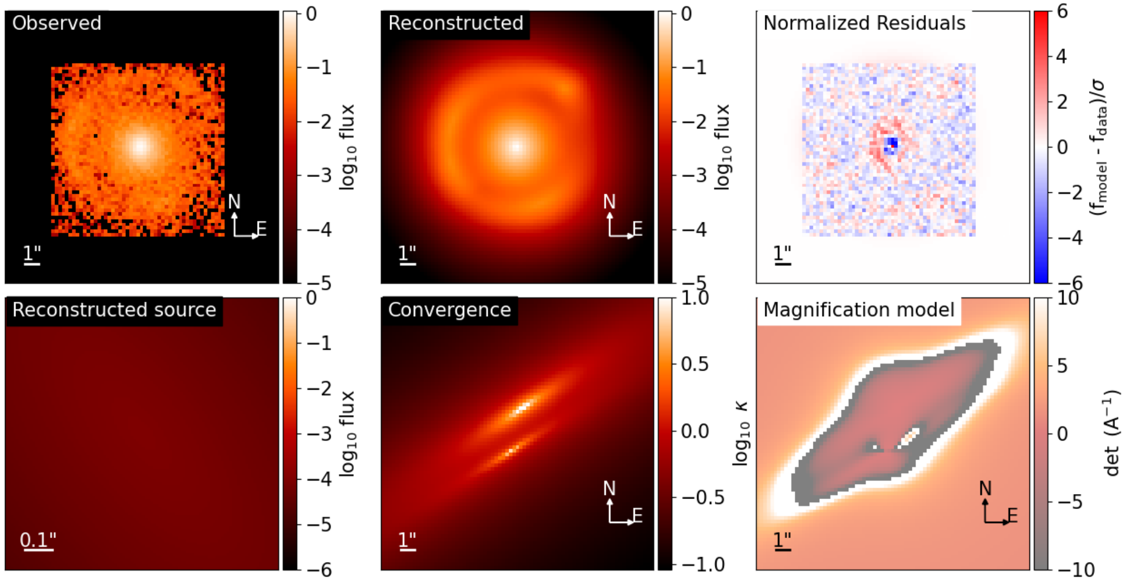

Figure A.11: 2SIE model, z-band: Comparison of observed and reconstructed images, as well as the residuals, reconstructed source, convergence and the magnification model for different image bands

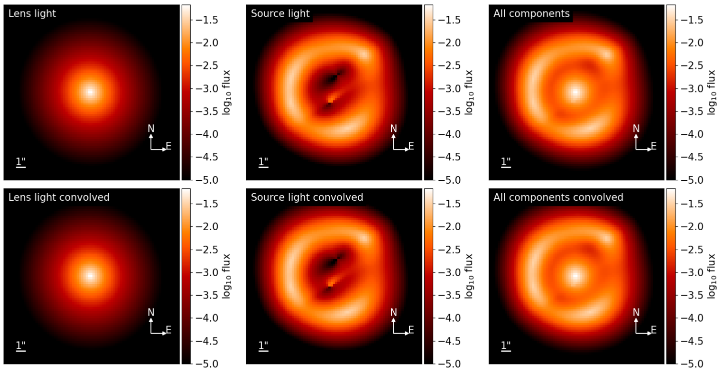

(a) *g*-band

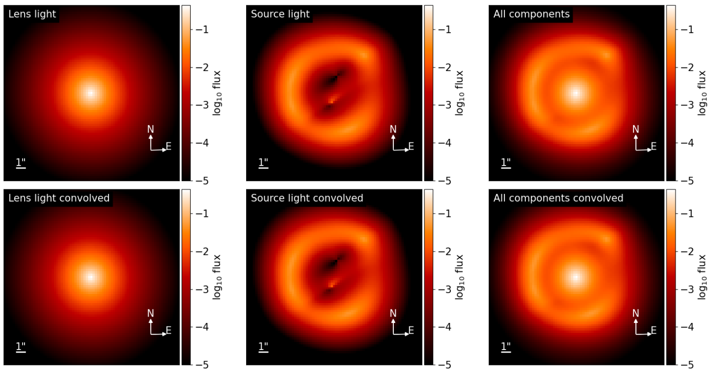

(b) *r*-band

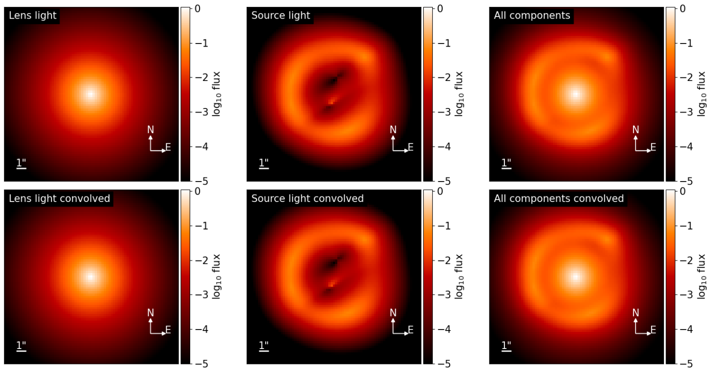

(c) *z*-band

Figure A.12: 2SIE model: Lens light, source lights and their convolutions for different image bands

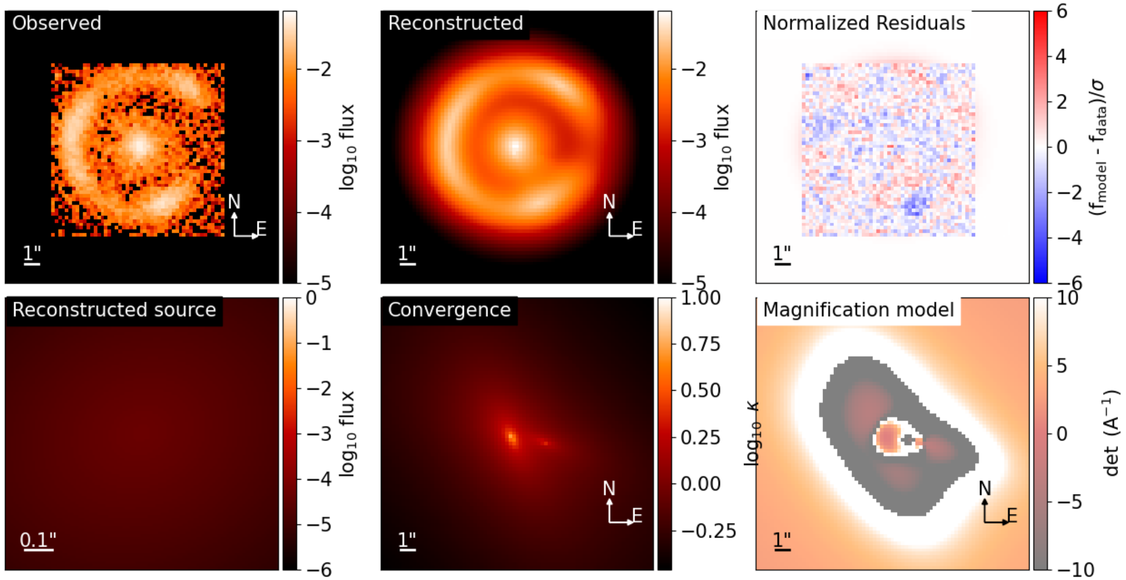

Figure A.13: 2EPL model, *g*-band: Comparison of observed and reconstructed images, as well as the residuals, reconstructed source, convergence and the magnification model for different image bands

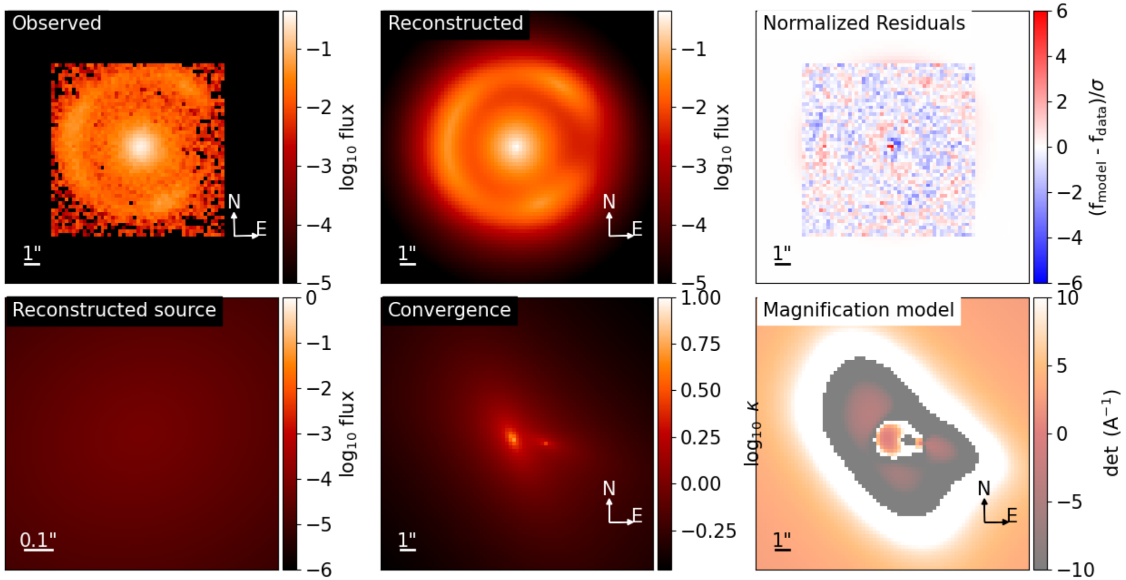

Figure A.14: 2EPL model, *r*-band: Comparison of observed and reconstructed images, as well as the residuals, reconstructed source, convergence and the magnification model for different image bands

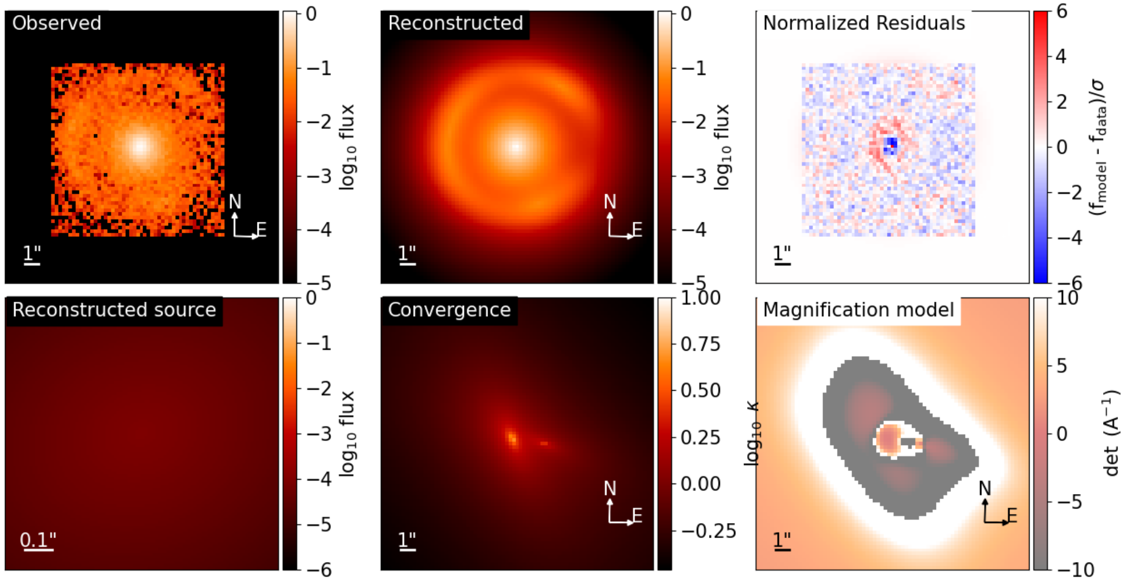

Figure A.15: 2EPL model, z-band: Comparison of observed and reconstructed images, as well as the residuals, reconstructed source, convergence and the magnification model for different image bands

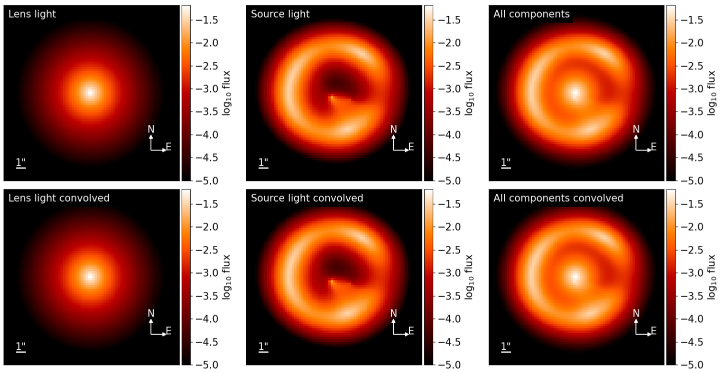

(a) *g*-band

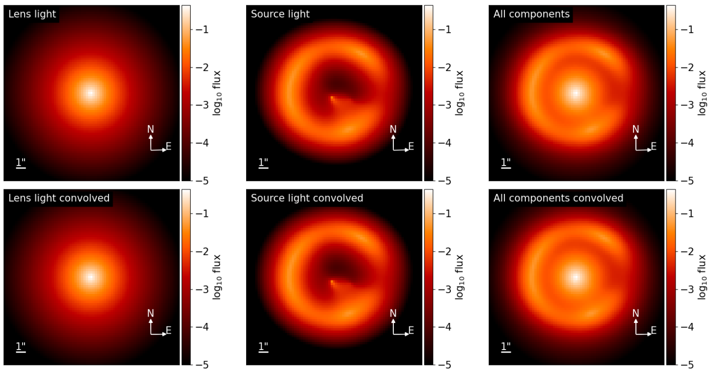

(b) *r*-band

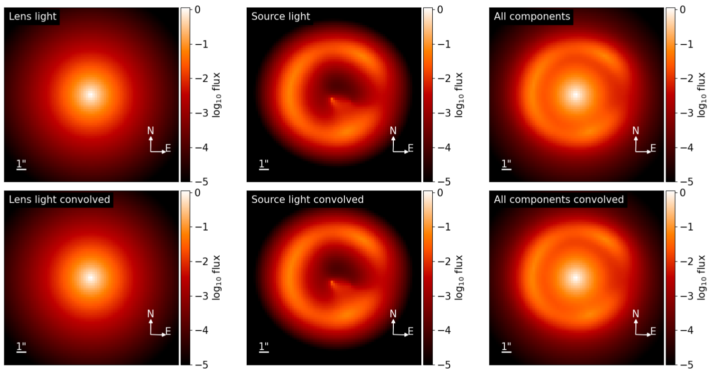

(c) *z*-band

Figure A.16: 2EPL model: Lens light, source lights and their convolutions for different image bands

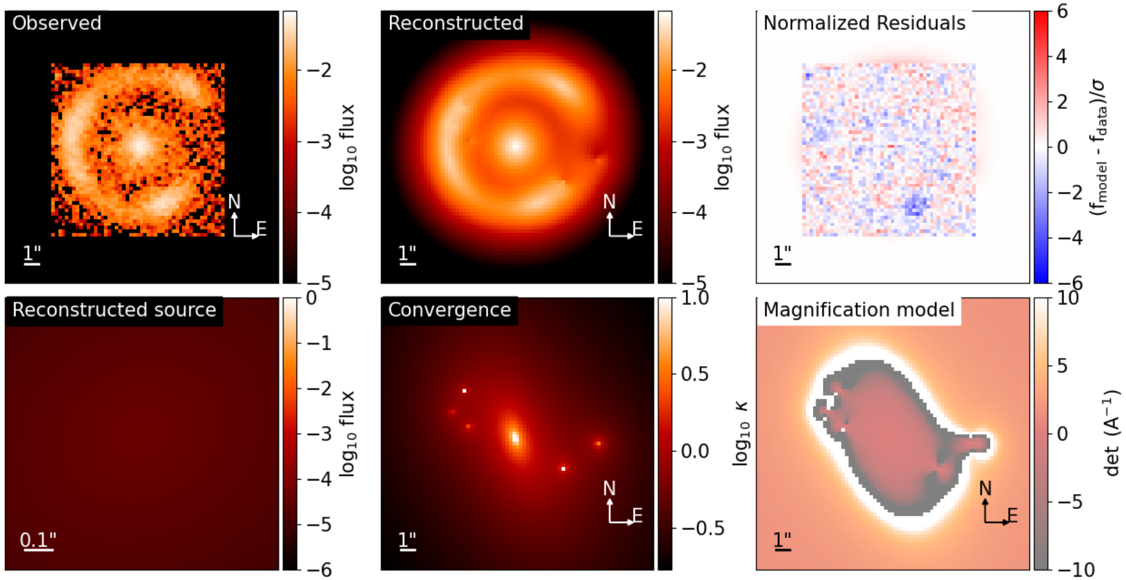

Figure A.17: SIE-5SIS model, g-band: Comparison of observed and reconstructed images, as well as the residuals, reconstructed source, convergence and the magnification model for different image bands

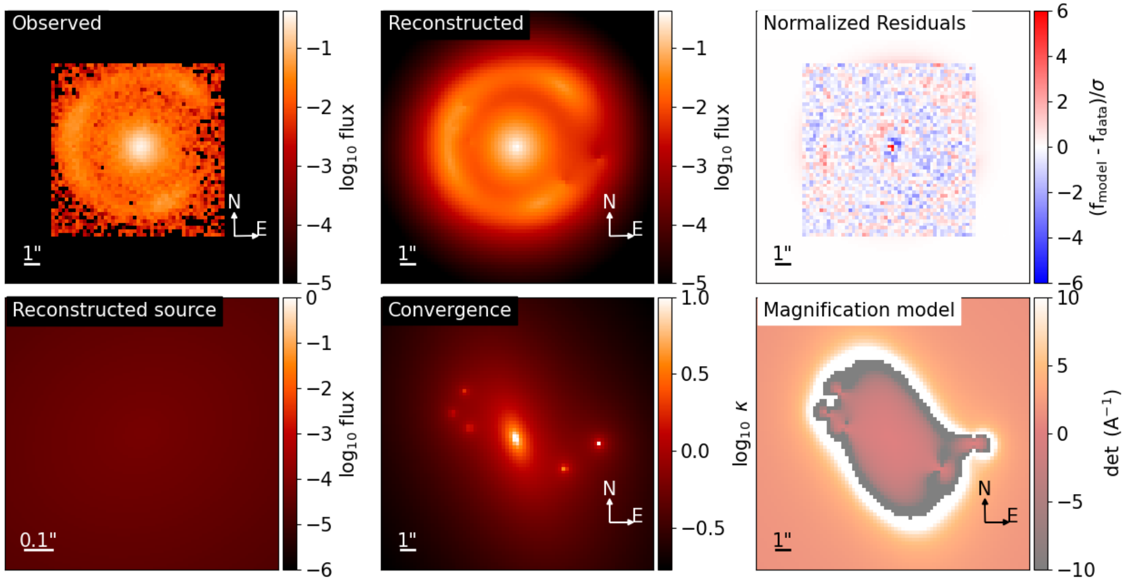

Figure A.18: SIE-5SIS model, *r*-band: Comparison of observed and reconstructed images, as well as the residuals, reconstructed source, convergence and the magnification model for different image bands

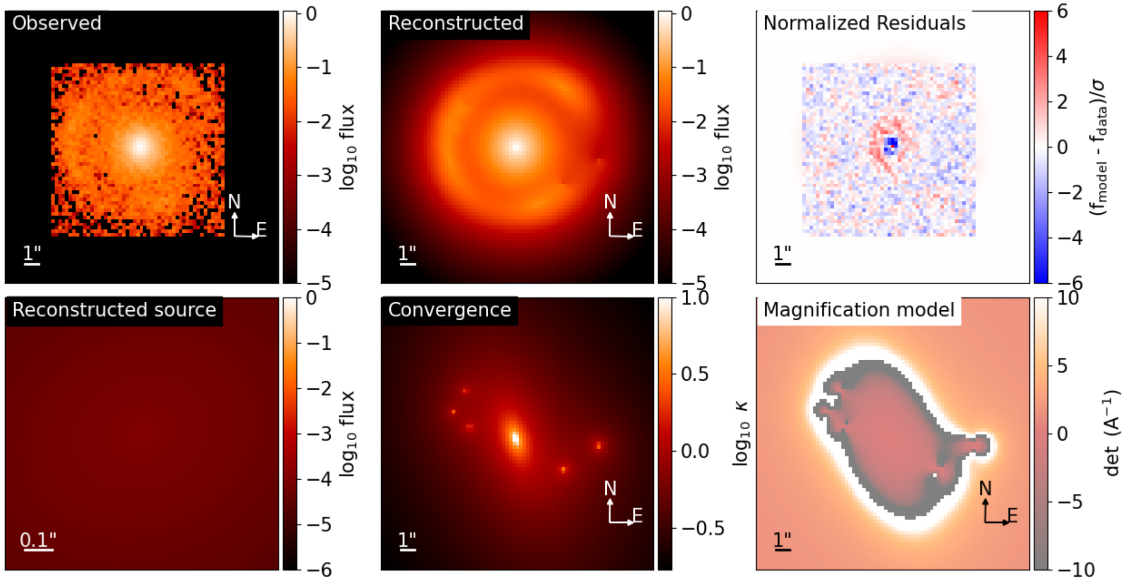

Figure A.19: SIE-5SIS model, z-band: Comparison of observed and reconstructed images, as well as the residuals, reconstructed source, convergence and the magnification model for different image bands

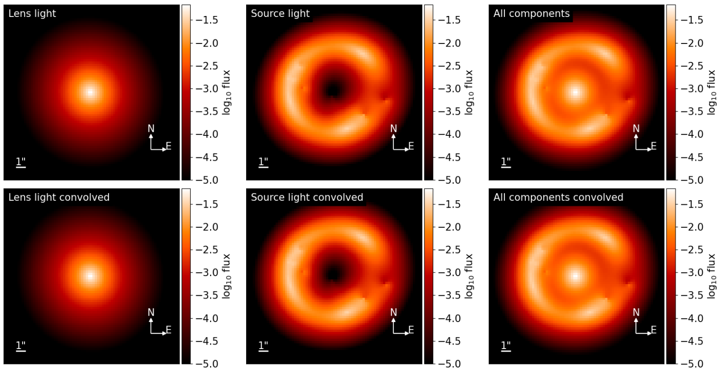

(a) g-band

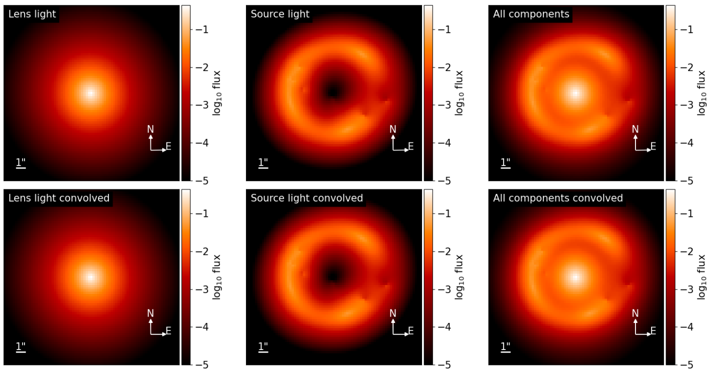

(b) r-band

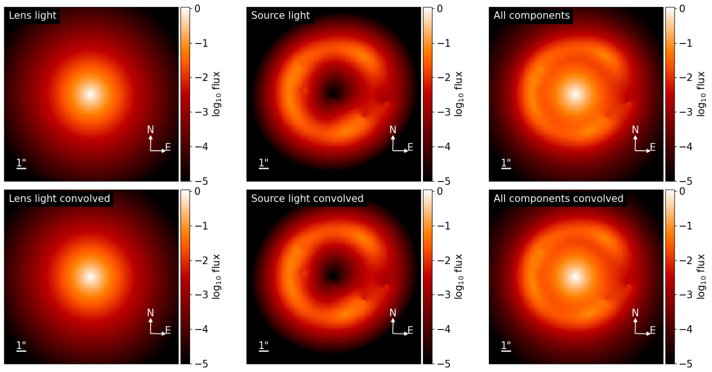

(c) z-band

Figure A.20: SIE-5SIS model: Lens light, source lights and their convolutions for different image bands

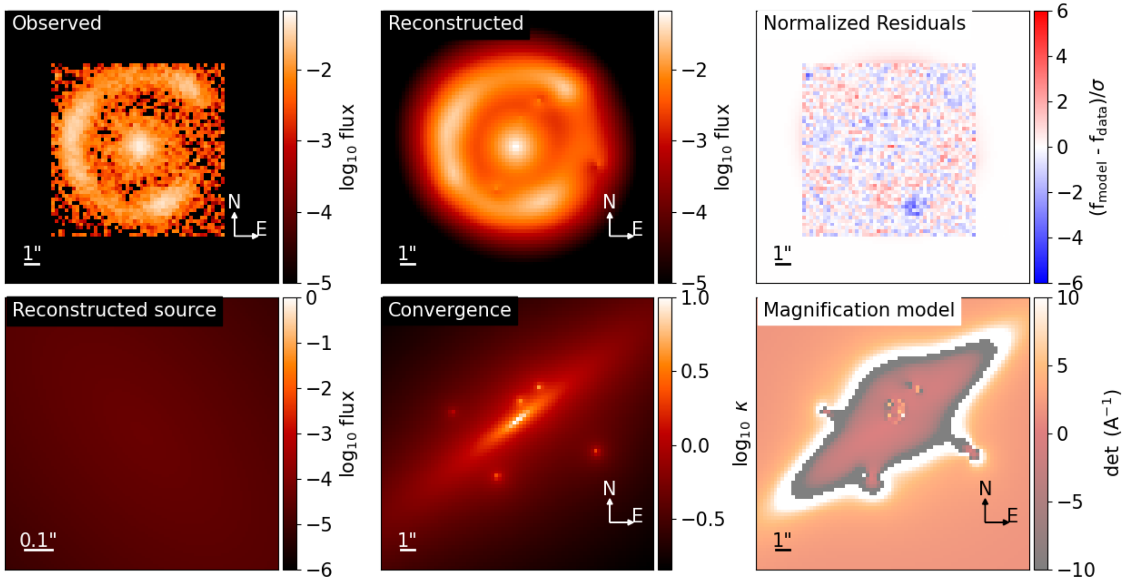

Figure A.21: EPL-5SIS model, *g*-band: Comparison of observed and reconstructed images, as well as the residuals, reconstructed source, convergence and the magnification model for different image bands

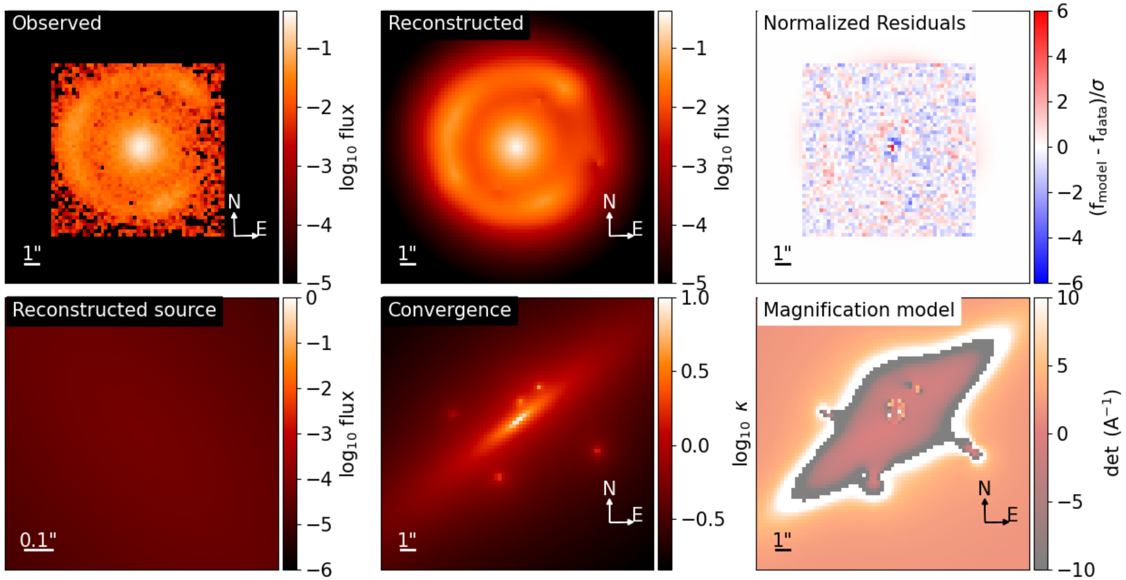

Figure A.22: EPL-5SIS model, *r*-band: Comparison of observed and reconstructed images, as well as the residuals, reconstructed source, convergence and the magnification model for different image bands

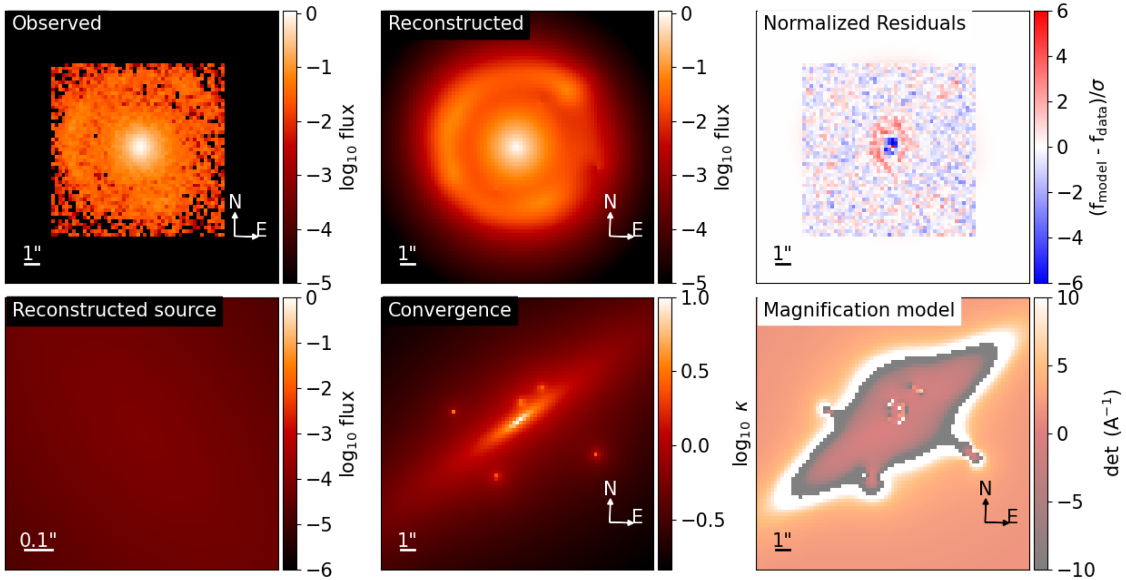

Figure A.23: EPL-5SIS model, *z*-band: Comparison of observed and reconstructed images, as well as the residuals, reconstructed source, convergence and the magnification model for different image bands

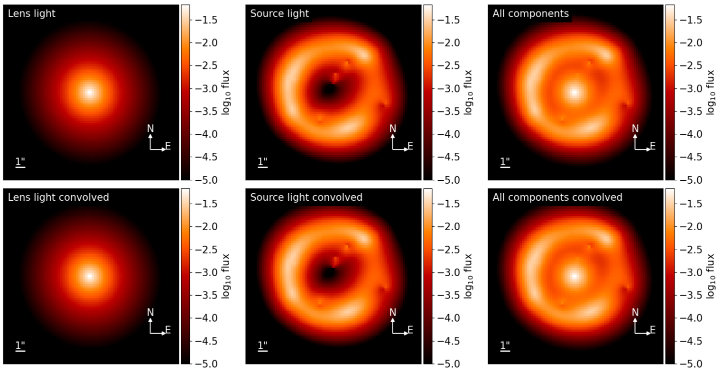

(a) *g*-band

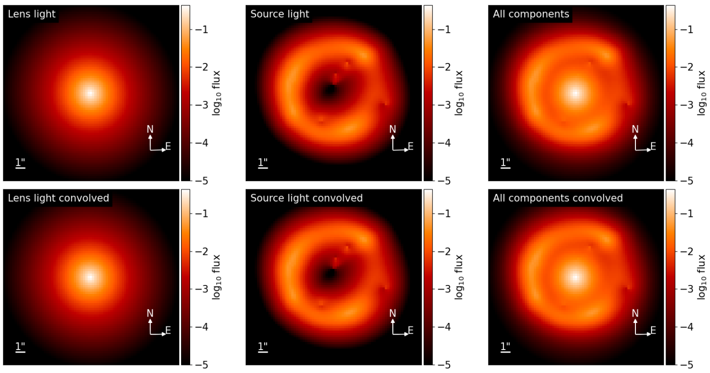

(b) *r*-band

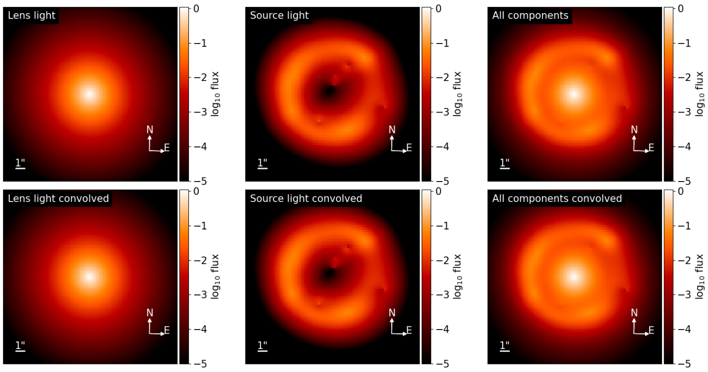

(c) *z*-band

Figure A.24: EPL-5SIS model: Lens light, source lights and their convolutions for different image bands

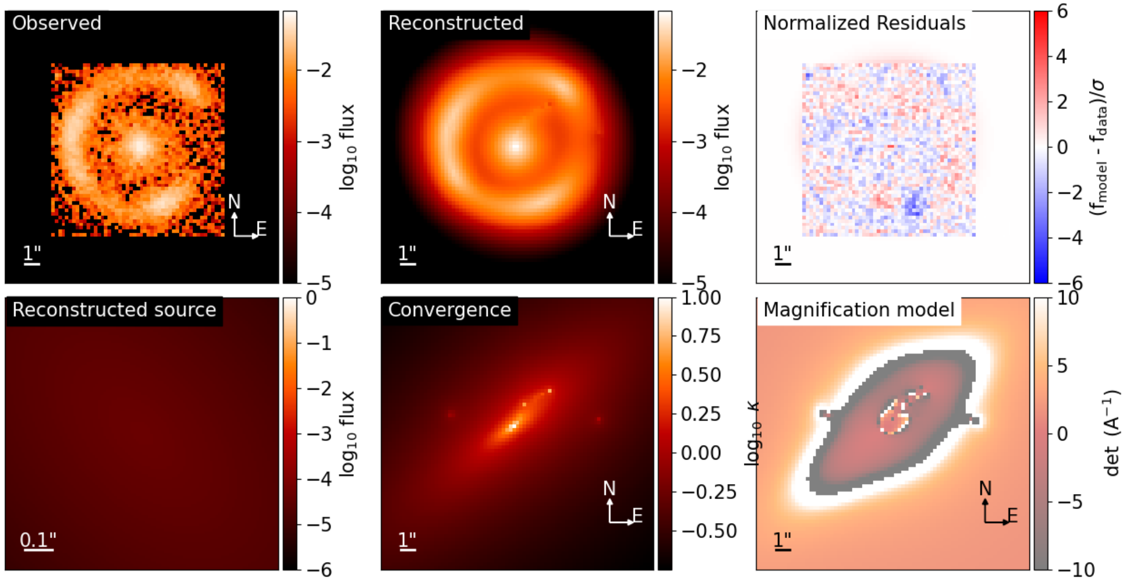

Figure A.25: EPL-50SIS model, g-band: Comparison of observed and reconstructed images, as well as the residuals, reconstructed source, convergence and the magnification model for different image bands

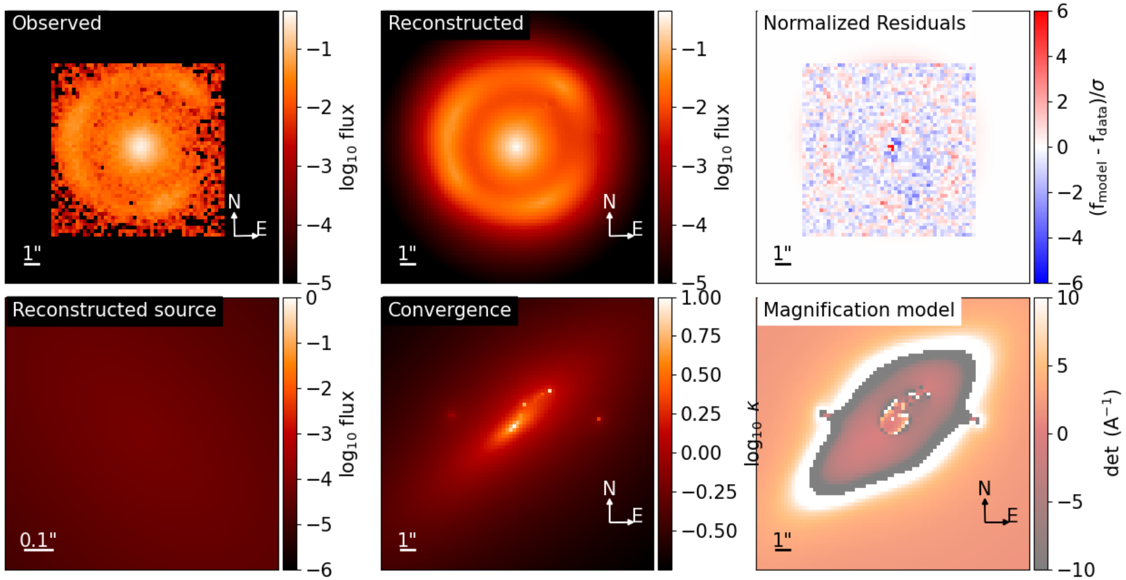

Figure A.26: EPL-50SIS model, r-band: Comparison of observed and reconstructed images, as well as the residuals, reconstructed source, convergence and the magnification model for different image bands

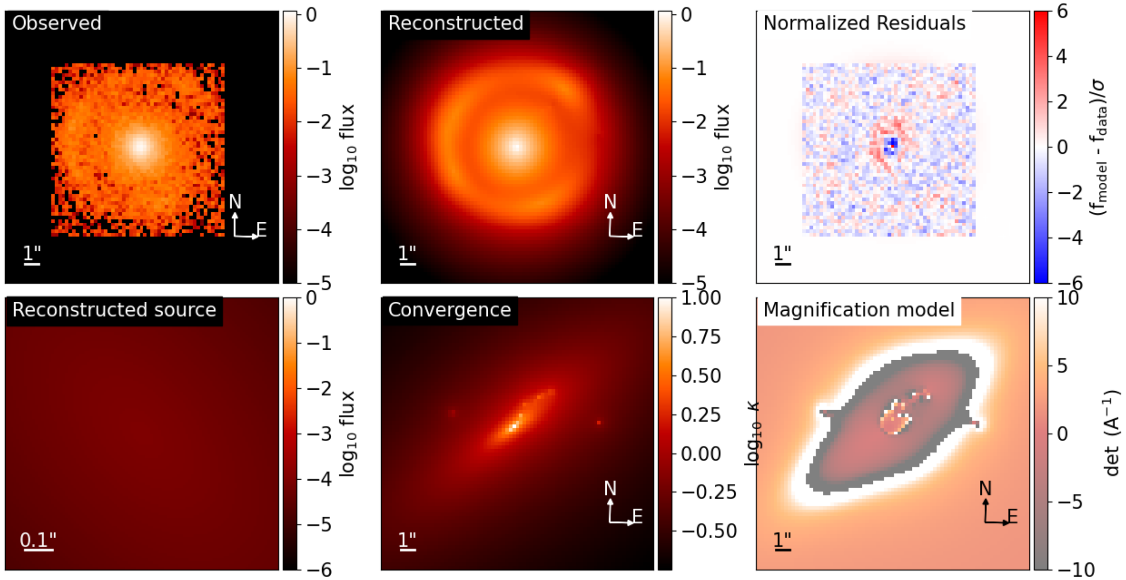

Figure A.27: EPL-50SIS model, *z*-band: Comparison of observed and reconstructed images, as well as the residuals, reconstructed source, convergence and the magnification model for different image bands

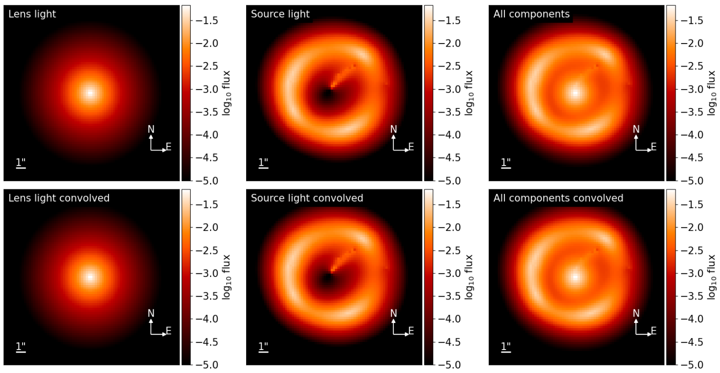

(a) g-band

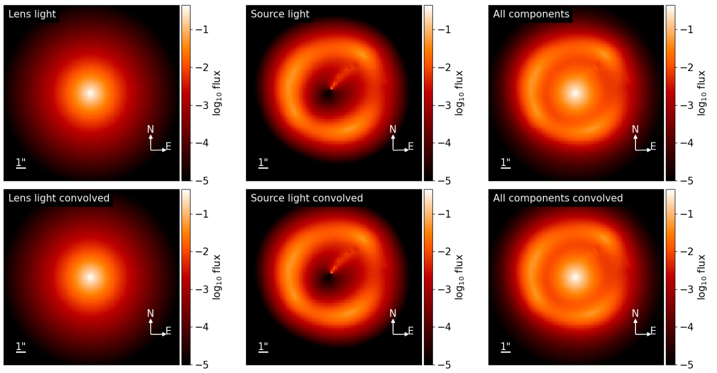

(b) r-band

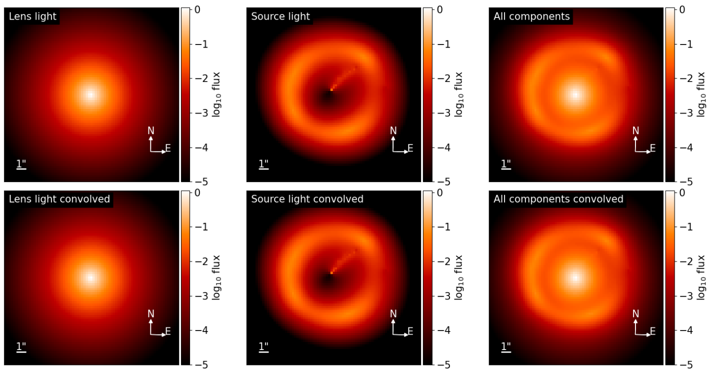

(c) z-band

Figure A.28: EPL-50SIS model: Lens light, source lights and their convolutions for different image bands